2013•2014
FACULTEIT GENEESKUNDE EN LEVENSWETENSCHAPPEN
master in de biomedische wetenschappen

Masterproef

Optical imaging of intracellular dynamics of nanoparticles in live cells

Promotor :
Prof. dr. Marcel AMELOOT

Copromotor :
dr. Rozhin PENJWEINI

Bart Wathiong

Proefschrift ingediend tot het behalen van de graad van master in de biomedische wetenschappen

De transnationale Universiteit Limburg is een uniek samenwerkingsverband van twee universiteiten in twee landen: de Universiteit Hasselt en Maastricht University.

universiteit hasselt
KNOWLEDGE IN ACTION

Universiteit Hasselt | Campus Hasselt | Martelarenlaan 42 | BE-3500 Hasselt
Universiteit Hasselt | Campus Diepenbeek | Agoralaan Gebouw D | BE-3590 Diepenbeek

universiteit hasselt | Maastricht University

2013•2014
FACULTEIT GENEESKUNDE EN LEVENSWETENSCHAPPEN
master in de biomedische wetenschappen

Masterproef

Optical imaging of intracellular dynamics of nanoparticles in live cells

Promotor :
Prof. dr. Marcel AMELOOT

Copromotor :
dr. Rozhin PENJWEINI

Bart Wathiong

Proefschrift ingediend tot het behalen van de graad van master in de biomedische wetenschappen

universiteit hasselt | Maastricht University

Acknowledgements

People say university days are the happiest of our lives. In the beginning it was very hard to believe, but now, while writing this thesis, I am looking back to five incredible years of which I will not regret one minute. During these years, I am introduced to the great world of science, of which I am now part of and wherein I am growing to become a skilled scientist. Therefore I hope this dissertation is not the end, but the start of a brand new scientific adventure. Since teamwork and cooperation are the fundaments of scientific research I would like to thank some people:

First of all I would like to thank my promoter, Prof. Dr. Marcel Ameloot, for the opportunity to do my senior project at the Biophysics research group. It was a privilege to learn from your knowledge and experience and a great pleasure to be part of the research group.

Next I want to express my appreciation to my co-promoter, Dr. Rozhin Penjweini, and to my supervisor, Dra Sarah Deville. You gave me an unforgettable time at the Biomedical research Institute. When you were around, all problems faded. Even during bad times, I could rely on you.

Also Dr. Nick Smisdom deserves a word of appreciation. Working together was a very pleasant experience. Your motivation is contagious and learning from you was an honour.

The next person I want to thank is Dr. Anitha Ethirajan. You taught me to evaluate my own work in a critical way. Together with your knowledge and advice I was able to improve my scientific skills.

Another person deserving many thanks is Dr. Patrick Vandormael. Although you were not a supervisor, I could always count on your help and your expertise.

Doing research on nanoparticles without nanoparticles is very hard. Therefore I would like to thank the Laboratory of Inorganic and Physical Chemistry led by Prof. Dr. Marlies Van Bael and Prof. Dr. An Hardy for supplying me with batches on nanoparticles. For the synthesis of these nanoparticles I would like to thank Wouter Vanoppré and Maarten Rubens and their supervisors, Dr. Ken Elen and Dr. Christopher De Dobbelaere.

Furthermore I want to express my appreciation to the Biomedical Research Institute for the opportunity to work in the well-equipped facilities and to the Biophysics group for the great time and the many patience.

Finally I want to thank my family and close friends. Although my adventure had both bad and good sides, I could always rely on them. Thank you for the endless support and trust in me.

Table of contents

List of abbreviations

AMPA	Aminomethylphosphonic acid
ATP	Adenosine triphosphate
CLSM	Confocal laser scanning microscope
DMEM	Dulbecco's modified eagle medium
EDTA	Ethylenediaminetetraacetic
FBS	Foetal bovine serum
FCS	Fluorescence correlation spectroscopy
FITC	Fluorescein 5(6)-isothiocyanate
GM	Geometric mean
ICS	Image correlation spectroscopy
IRF	Instrument response function
KDP	Potassium dihydrogen phosphate
LCl	Lower confidence level
LDH	Lactate dehydrogenase
LSM	Laser scanning microscope
MEM	Modified eagle medium
MTS	3-(4,5-dimethylthiazol-2-yl)-5-(3-carboxymethoxyphenyl)-2-(4-sulfophenyl)-2H-tetrazolium
NPs	Nanoparticles
PBS	Phosphate-buffered saline
PMT	Photo multiplier tube
R6G	Rhodamine 6G
RICS	Raster image correlation spectroscopy
SHG	Second harmonic generation
STICCS	Spatio-temporal image cross-correlation spectroscopy
STICS	Spatio-temporal image correlation spectroscopy
TICS	Temporal image correlation spectroscopy
UCl	Upper confidence level

Abstract

Nanotechnology and nano-applications are emerging in science and in society. Despite their (future) role in many applications, not much is known about their effects on living organisms. In order to establish potential hazards to health, knowledge of the perturbation induced by nanoparticles (NPs) on basic cellular functions is essential. The mechanism by which NPs enter and are transported within the cell predominantly determines their intracellular fate and, consequently, their biological impact. In the present study, label-free live-cell imaging techniques were applied to investigate the cellular trafficking of harmonic NPs within human lung epithelial cells *in vitro*. The unique properties of these nanomaterials allow for prolonged observation times without photobleaching or inducing phototoxicity, which permits exploring complex intracellular transport modes. Temporal image correlation spectroscopy (TICS) and spatio-temporal image correlation spectroscopy (STICS) were performed to investigate the intracellular NP motions, whereas spatio-temporal image cross-correlation spectroscopy (STICCS) was used to provide information about the kinetics of co-localization with lysosomes. Insights in NP transport modes contribute to elucidate the cellular pathways, which take place after NP exposure, and their possible interference with normal cell function.

Besides image correlation spectroscopy, fluorescence anisotropy can be employed to investigate rotational motions of NPs. Since this study is the first time anisotropy measurements are implemented on the confocal microscope of the host group, the experiments are limited to testing and optimization of the analysis procedure. Besides proof-of-principle tests with rhodamine 6G dissolved in glycerol, also influences caused by the system were analysed. Depolarizing effects from the dichroic mirror were measured. Moreover, the rotation of the removable detectors as well as the differential sensitivity between both detection channels was evaluated. All these parameters need to be taken into account for the calculation and fitting of the fluorescence anisotropy. Human lung fibroblasts were used, in combination with fluorescently labelled polymers, for a more applied experiment. Rotational motions were studied using fluorescence anisotropy and were compared to the free moving labels.

When the method of fluorescence anisotropy is fully optimized for this system, insights in rotational motions can complement the data of intracellular dynamics obtained via image correlation spectroscopy (ICS). If this study is successful, results will be of major importance in medicine to improve drug delivery systems, but also in the safe nano-product development.

Samenvatting

Nanotechnologie en hierop gebaseerde toepassingen kennen een sterke toename, zowel in het wetenschappelijk landschap als in de samenleving. Ondanks hun (toekomstige) rol in vele toepassingen is er slecht weinig geweten over hun effecten op levende organismen. Om potentieel schadelijke gezondheidseffecten in kaart te brengen, is kennis over hoe nanopartikels (NPs) basis cellulaire functies verstoren essentieel. Het mechanisme waarmee NPs door cellen opgenomen en getransporteerd worden is de voornaamste factor die hun lot en bijgevolg hun biologische impact zal bepalen. In deze studie werden label-vrije beeldvormingstechnieken aangewend om het transport van harmonische NPs in humane long epitheelcellen te bestuderen. De unieke eigenschappen van deze nanomaterialen zorgden ervoor dat het complexe intracellulaire transport onderzocht kon worden zonder dat er effecten zoals fotobleking of fototoxiciteit optraden. Met behulp van microfluorimetrische technieken zoals *temporal image correlation spectroscopy (TICS)* en *spatio-temporal image correlation spectroscopy (STICS)* werden de intracellulaire bewegingen van de NPs bestudeerd. Verder werd er door middel van *spatio-temporal image cross-correlation spectroscopy (STICCS)* informatie over de kinetica en co-lokalisatie met lysosomen verkregen. De verworven inzichten in intracellulair transport dragen bij aan de verduidelijking van de cellulaire processen die plaatsgrijpen na blootstelling aan NPs. Bovendien zal het een licht werpen op de verstoring van het normaal functioneren van de cel. Naast de *image correlation spectroscopy* technieken, werd er in deze studie ook gebruik gemaakt van fluorescentie-anisotropie om de rotatie van de NPs te bestuderen. Omdat deze studie draaide rond de implementatie van fluorescentie-anisotropie in de microscoopopstelling van de onderzoeksgroep zijn de experimenten beperkt tot het testen en optimaliseren van de meetprocedures. Naast de basisimplementatietesten met rhodamine 6G in glycerol werden ook de systeemeffecten geanalyseerd. Na het meten van de depolariserende effecten van de dichroïsche spiegel, werd het effect afkomstig van het roteren van de afneembare detector bepaald. Verder werd het verschil in gevoeligheid tussen de twee detectiekanalen nagegaan. Al deze parameters moeten in rekening gebracht worden bij het berekenen van de fluorescentie-anisotropie. Voor een meer toegepast experiment werd er gebruik gemaakt van humane long fibroblasten en polymeren voorzien van een fluorescent label. Door middel van fluorescentie-anisotropie werden de rotatie-bewegingen van de labels bestudeerd. Als de techniek van fluorescentie-anisotropie volledig geïmplementeerd is kunnen de inzichten in rotatie van moleculen bijdragen aan de studie van de intracellulaire dynamica. Een succesvolle studie kan van groot belang zijn in zowel de geneeskunde om *drug delivery systems* te verbeteren, als in de ontwikkeling van veilige nano-producten.

1 Introduction

Nanotechnology is a scientific field comprising the development, synthesis and application of matter whose size and shape are manipulated at the nanoscale[1]. Nanoparticles (NPs) are defined as particles with at least one dimension between 1 and 100 nm[2]. Due to their small dimensions, NPs have a high surface-to-volume ratio differentiating them from bulk material. NPs possess a different chemical reactivity, as well as altered mechanical, electric, magnetic and optical properties, all induced by surface and quantum effects. Their distinct intrinsic physiochemical properties, compared to bulk material, are the main reason for the popularity of addition of NPs in a wide range of applications such as paintings, cosmetics, tires, food additives etc.[1]. Because nano-sized materials and NPs are emerging and very promising, they also appear more and more in biomedical tools where they have a prominent role.

1.1 Cellular uptake and transport

As nanotechnology is growing extremely fast and NPs find their way to applications in daily life, hazardous health impacts have to be considered. Because NPs are of comparable size as biomolecules, they are potentially able to enter a living cell. This is an important property that can be very helpful in diagnostics and therapeutics, but despite the advantages NPs are able to exert adverse health effects. Although not much is known about the effects of engineered NPs on living organisms [3, 4] and literature has not documented clinical toxicity thus far, it is already been proven that incidental nano-sized particles such as asbestos, diesels exhaust particles and ultrafine particles exert negative effects on human health[5].

In order to compose safety standards and to optimize nanoparticle-based applications, knowledge about the interactions between NPs and biological systems is needed. Little is known about the processes occurring when NPs are exposed to biological fluids, clearing mechanisms, phospholipid bilayers and intracellular conditions[4]. Therefore it is a challenge to predict the mechanism of NP uptake. To enter a cell, NPs have to cross the cellular membrane. This phospholipid bilayer regulates the transport of molecules into the cells and is an important defence-mechanism to protect intracellular structures. Polar or charged particles require active transport in order to enter a cell. Therefore, many molecules are internalized via a vesicular transport mechanism. To be actively transported, endocytosis comes into play. Endocytosis can be defined as the formation and inward cytosolic movement of plasma membrane vesicles[6]. This internalization process constitutes of different pathways. Depending on their dimensions, particles are internalized either via pinocytosis (<0.5 µm) or via phagocytosis (>0.5 µm). Pinocytosis can be further subdivided in four pathways: actin-driven membrane protrusion, clathrin coated vesicles (120 nm),

caveolae (50-80 nm) and clathrin and caveolin independent uptake[7, 8]. Besides uptake mechanisms, modes of transport also determine the intracellular fate of internalized particles. The cytoskeleton, composed of microtubules, actin filaments and intermediate filaments is an important element during cellular transport. The microtubules and actin filaments have a prominent role in intracellular transport: besides regulation of membrane traffic, actin filaments and microtubules serve as a track for organelles to displace. Furthermore, actin polymerization generates membrane-invagination, coated-pit formation, conscription and vesicle scission during clathrin-mediated endocytosis[6, 9]. In mammalian cells actin even contributes in the internalization of caveolae. All internalized particles travel to the early endosomes to reach the late endosome. Yet, it is still unknown how the caveosomes reach the early endosomes. The late endosomes destined for degradation will travel to the lysosomes whereas other particles will be recycled via the plasma membrane or via the Golgi apparatus. The transport of endocytosed particles and the fusion between early and late endosomes require both an intact network of microtubules. Furthermore, the lysosomes travel along the microtubule network, and recent studies have shown that F-actin and myosins might be involved in this movement controlling the routes travelled by the organelles on the microtubules[4, 9]. In order to establish potential hazards to health, knowledge of the perturbation induced by NPs on basic cellular functions is essential. The mechanism by which NPs enter and are transported within the cell predominantly determines their intracellular fate and, consequently, their biological impact. Therefore, the investigation of the cellular uptake mechanisms and cellular trafficking is of major importance. The aim of this project is to get more insights in the transport and dynamics of NPs within biological systems. An important element of the cytoskeleton that provides cellular transport is the microtubules. Because NPs are transported by these mechanisms, effects by exposure are expected. Previous studies have already demonstrated that NPs can decrease polymerization of microtubules[10]. Microtubules play an important role during cell division and serve as a scaffold in cellular uptake and transport[11]. This means that any effect on microtubules will also influence cell-functionality. Besides the microtubule and cytoskeleton, NPs also disrupt synaptic machinery of cortical neurons[12]. Furthermore, adhesion, morphology and cytoskeleton organisation of human fibroblast can be altered by gelatin NPs[13].

In the present study, the behaviour of NPs in cells will be studied by means of optical imaging techniques. To this end two different techniques are employed: image correlation spectroscopy (ICS) of second harmonic generating (SHG) $BaTiO_3$ NPs on one hand, and fluorescence anisotropy of fluorescently labelled polymers on the other hand. Since it is the first time the technique of fluorescence anisotropy mapping is implemented on the confocal microscope of the host group, the main focus for this aspect is on optimizing the system and the procedure.

1.2 Barium titanate nanoparticles

Due to low cost and low nanotoxicity in biological cells, together with the ease of synthesis, tetragonal barium titanate ($BaTiO_3$) is an interesting material for SHG microscopy[14]. Barium titanate is widely used in electric applications. Its high dielectric constant and its ferroelectric response make that it is extensively used in industrial applications such as switches, sensors and multilayer ceramic capacitors[15, 16]. Besides (di-)electric applications, $BaTiO_3$ NPs also possesses features for biological applications.[17] Nanovectors and bioconjugated nanocrystals for microscopy probes are the main applications studied so far[17, 18]. In this study, tetragonal $BaTiO_3$ (*figure 1*) will be used to investigate the intracellular dynamics and fate of NPs.

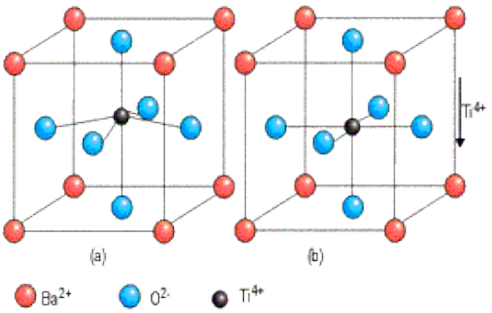

Figure 1: Tetragonal $BaTiO_3$ vs. cubic $BaTiO_3$[19]

1.3 Fluorescently labelled polymers for anisotropy measurements

The method of fluorescence anisotropy will be used in live cell experiments, using polymers labelled with BiB-fluorescein or fluorescein acrylate (Appendix section 6.1). These polymers are obtained from the Interfaculty Centre of Biomaterials from the University of Liège and due to their confidential nature information is limited.

1.4 Optical imaging techniques suitable for monitoring NP dynamics

To visualize and study the cellular travelling of the NPs, fluorescence microscopy, and more specifically image correlation spectroscopy, will be employed. Despite time-lapse fluorescence microscopy is very useful and very sensitive, some important disadvantages such as photobleaching and blinking, can restrict the application of this technique. The problem of photo-bleaching is the limitation in the total number of photons that can be emitted by a dye, resulting in a decrease in observation time[20]. To circumvent these problems, fluorescent dyes are replaced by SHG particles, possessing unique properties making them very promising for live-cell imaging purposes[20].

1.4.1 SHG microscopy

SHG is a second-order non-linear optical process based on the simultaneous excitation of a molecule by two photons. This phenomenon can only be applied to non-centrosymmetrical materials, which means they have no mirror symmetry. When two photons at frequency ω interact with this material they are combined to one photon with twice the energy and twice the frequency (2ω)[20, 21]. Therefore, the second-harmonic light emitted by the material is at exactly half the wavelength of the excitation wavelength, i.e. the initial two photons. In contrast to two-photon excitation, where the molecule is excited to an excited state, SHG involves a virtual electron energy transition, without loss of non-radiative energy[22]. This virtual transition process entails some important advantages: SHG active crystals are not subject of bleaching over time and they emit a stable, non-saturating signal with a response time at the femtosecond time scale as this is essentially a scattering process. This enables investigation of fast dynamic processes over a long observation time[22]. On the other hand, the similarity between SHG and two-photon fluorescence is that both their emission intensity depends on the square of the excitation intensity[21].

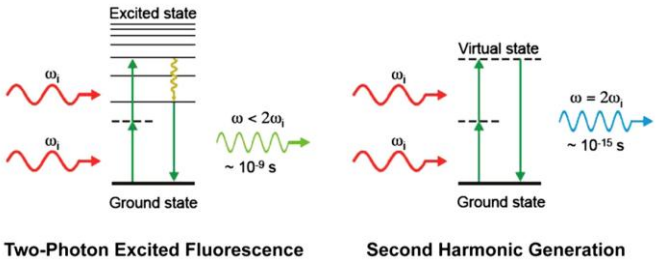

Figure 2: Two-photon excited fluorescence versus second harmonic generation. *Both processes start with excitation by two photons, but SHG involves only a virtual state in contrast to the excited transition state of two-photon excitation fluorescence[20].*

Moreover, (nano)materials can be excited by a two-photon pulsed laser. Therefore the imaging will be less invasive and less damaging due to the higher wavelength of the infrared photons[18, 20]. All these properties are of major importance when studying complex intracellular transport modes.

1.4.2 Image correlation spectroscopy

Fluorescence correlation spectroscopy (FCS) is one of the most successful microscopy methods for quantitative analyses inside living cells[23, 24]. In the 1970s, FCS was developed to measure macromolecular transport properties and concentrations. Here, a temporal autocorrelation analysis of the amplitude and temporal characteristics of the fluorescence signals measured in a tiny focal volume is performed[25]. However, currently this technique has been extended with multiple analogues. One of these analogues, image correlation spectroscopy (ICS) was introduced by Petersen et al. (1993) and is predominantly used during this study[26]. ICS is based on spatial correlation analysis of fluctuations in the

fluorescence signal within an image or image series. The fluctuation of the fluorescence intensities are measured in the diffraction-limited focal spot of the laser beam used in a confocal laser scanning microscope (CLSM)[24]. Depending on the variant of ICS, correlation functions in one or both domains of space and time are used to analyse the measured intensity fluctuations. From the spatial sampling, it is possible to obtain information about the percentage of the immobile population (e.g. concentration and aggregation state)[26, 27]. From the analysed intensity fluctuations, information regarding transport dynamics (diffusion, flow, etc.) of the fluorophores can be obtained. For instance, variations in static or slowly moving fluorophores are reflected by the spatial intensity fluctuations. Fluorophores undergoing transport or non-stationary emission photophysics generate dynamic changes in the number of fluorophores detected in a given spot over time resulting in temporal intensity fluctuations[27].

Because a tiny focal volume is used to detect fluorescence signals, one has to note that the intensity from such a point source will be spread out in three dimensions upon detection due to diffraction. The point spread function (PSF) of the microscope contains the spatial extent of the diffraction pattern and will be a Gaussian[27]. ICS is a spectroscopic technique with multiple variants, differentiated from each other by the correlations in time and space. ICS variants treated here are: spatiotemporal image correlation spectroscopy (STICS), spatiotemporal cross-correlation spectroscopy (STICCS), temporal image correlation spectroscopy (TICS) and raster image correlation spectroscopy (RICS). Originally spatial and temporal correlations were treated separately[24]. Temporal and spatial intensity fluctuations can be combined in spatiotemporal correlation functions, as is used in STICS. STICS is an imaging technique to detect diffusion and flow of molecules over the cellular membrane as well as the percentage of mobile proteins present in the sample. In contrast to FCS, STICS measures slow dynamics of the molecules of interest. STICS can be further extended by combining it with cross-correlation. In spatiotemporal image cross-correlation spectroscopy (STICCS), the spatiotemporal autocorrelation function of STICS is combined with the dual-labelled sample and dual channel technique. In this technique, the molecules are labelled independently with two spectrally separated fluorescent dyes. The labelled molecules are either excited simultaneously with the same laser or by two different lasers separately. The fluorescence emission is measured with two different detectors[28]. In this way, information about the rate of diffusion, speed and direction of flow and the percentage of mobile particles can be obtained. Even, due to the cross-correlation, it is possible to determine if particles diffuse or move together[28]. TICS is a technique developed to measure the diffusion coefficient and flow speed from an image time series of slow moving membrane proteins. This is possible because time correlation functions are sensitive to moving fluorescent particles, present within the focal spot of the laser beam for a number of image frames.

Raster image correlation spectroscopy (RICS) is a recent technique developed to extract information about molecular dynamics and concentrations from confocal images. As in ICS, RICS is based on the detection of intensity fluctuations within a focal volume in a biological system. These fluctuations can arise from different events for instance conformational changes, binding to immobile or larger structures or just entering or leaving the focal volume. Analysis of the RICS images reveals information about dynamics and aggregation states of particles, but will not be carried out in this study[29]. The ICS techniques described above are based on fluorescence. However in present study they will be applied using the SHG signals from the NPs. Therefore adjusted expressions are required. But because the experiments are about the feasibility of ICS using SHG, these expressions are not discussed.

1.4.3 Fluorescence anisotropy

Fluorescence techniques are optimally suited and are therefore mostly used to measure protein dynamics[30]. An important part of intracellular dynamics is the presence of rotational motions of particles in the cell. This rotational diffusion is sensitive to changes in molecular size and establishes therefore parameters with very high sensitivity[31]. The rotational motions of free molecules in solution are in the order of nanoseconds, but in cellular compartments the molecules experience a viscous friction caused by the microenvironment which will lead to a rotational motion in the microsecond range[31]. To analyse rotational motions fluorescence anisotropy can be used because a high precision is possible with modern laser-based time-resolved fluorescence techniques. Fluorescence excitation involves the absorption of a photon by the fluorophore to excite an electron to a higher energy level. This electron excitation creates a dipole moment.

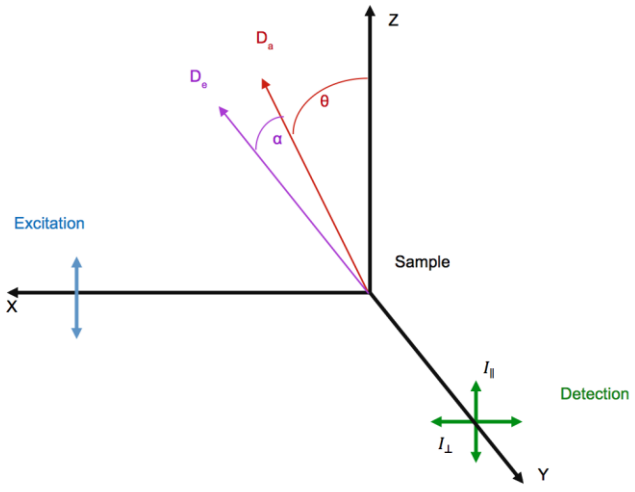

Figure 3: Coordinate system showing basic quantities of fluorescence anisotropy. *The sample is at the origin and excited by polarized excitation light. The electric vector of the excitation light is oriented along the Z-axis. Polarized emission is detected using perpendicular and parallel detection. The absorption dipole moment (D_a) and emission dipole moment (D_e) are intrinsic properties of the fluorophore.*

The orientation of this absorption dipole, together with the electric field orientation of the excitation light determines the probability that a fluorophore will be excited (*figure 3*). The excitation probability is the highest when both electric field and absorption dipole are parallel, and is the lowest when they are perpendicular[32, 33]. The excitation probability is given by $cos^2\ \theta$ with θ being the angle between the electric field vector and the absorption dipole (*figure 3*). The process of *photoselection* is based on this probability: when a population of randomly oriented fluorophores is irradiated with linearly polarized excitation light, only those with the absorption dipole orientations similar to the electric field orientation will be preferentially selected. Next to an absorption dipole, an emission dipole can be defined for a fluorophore. If the absorption and emission dipoles have equal orientations, they are said to be collinear, if not, the emission dipole determines the orientation of the electric field of the emission light.

Anisotropy (r) is the intensity ratio of the polarized component to the total intensity[32]. Hence fluorescence anisotropy is a measure of emission polarization and constitutes of two emission components: parallel ($I_{\parallel}$) and perpendicular ($I_{\perp}$) both measured with respect to the electric vector of linearly polarized incident light[34]. Therefore the fluorescence anisotropy is given by

$$r = \frac{I_{\parallel} - I_{\perp}}{I_{\parallel} + 2I_{\perp}} \tag{1}$$

where r is the fluorescence anisotropy and the denominator represents the total emission intensity, the sum of the three orthogonal emission components[31, 33, 34]. In former studies and publications polarization is used more often. Since polarization and anisotropy contain the same information, anisotropy is preferably used because it is normalized by the total intensity ($I_{\parallel} + 2I_{\perp}$)[34].

1.4.4 Time-dependent anisotropy decays

In steady-state fluorescence anisotropy measurements samples are illuminated with constant illumination. Time-dependent anisotropy analysis provides additional temporal information following pulsed excitation. The characteristics of the molecule of interest (size, shape and flexibility) determine the shape of the anisotropy decay. Using infinitely short pulses of polarized excitation light, time-resolved fluorescence anisotropy $r(t)$ can be calculated by:

$$r(t) = \frac{i_{\parallel}(t) - i_{\perp}(t)}{i_{\parallel}(t) + 2i_{\perp}(t)} \tag{2}$$

where $i(t) = i_{\parallel}(t) + 2i_{\perp}(t)$ is the total time-resolved fluorescence intensity $i(t)$[34]. The time evolution of the polarized fluorescence can be obtained for each polarized component:

$$i_{||}(t) = \frac{i(t)}{3}\left[1 + 2r(t)\right] \tag{3}$$

$$i_{\perp}(t) = \frac{i(t)}{3}\left[1 - r(t)\right] \tag{4}$$

In general, $r(t)$ is given by a linear combination of exponentially decaying functions:

$$r(t) = \sum_{j=1}^{m} \beta_j \exp\left(-t/\theta_j\right) \tag{5}$$

with θ_j being the rotational correlation times. For spherical rotors: $m = 1$. The fundamental anisotropy, r_0 included in Eq. (5) is given by $\sum_{j=1}^{m} \beta_j$. For ellipsoids, rotational correlation times are dependent on the diffusion constants for rotation around the ellipsoid symmetry axis ($D_{\parallel}$) and around the axis perpendicular to the ellipsoid symmetry axis ($D_{\perp}$). The rotational correlation times are function of the hydrodynamic volume of the rotor, as well as the temperature and viscosity of the solvent. However, they are independent of the wavelengths of excitation and emission light[35]. In practice, if the width of the excitation pulse is much smaller than the decay times, experimental decay curves of the polarized components can be used to calculate the emission anisotropy:

$$r(t) = \frac{I_{\parallel}(t) - GI_{\perp}(t)}{I_{\parallel}(t) + 2GI_{\perp}(t)} \tag{6}$$

$$G = \frac{S_V}{S_H} \tag{7}$$

where G is the factor to correct for the differential sensitivity of the detection channels and is simply the ratio of the sensitivity of the detection system for vertically and horizontally polarized light. S_V and S_H are the sensitivities of the emission channel for the vertically and horizontally polarized components. The parallel and perpendicular polarized fluorescence decay curves $I_{\parallel}(t)$ and $I_{\perp}(t)$ are convolution products of the instrument response function of the confocal setup used.

The fundamental emission anisotropy r_0 refers to a situation in which depolarization occurs only due to the angle between the absorption and emission transition moments. Therefore, the fundamental emission anisotropy for two photon excitation can be described by:

$$r_0^{(l)} = \frac{2l}{2l+3}\left[\frac{3}{2}cos^2\alpha - \frac{1}{2}\right] \tag{8}$$

with α being the angle between the absorption and emission transition moments, l being the amount of photons absorbed in the same quantum event. For collinear transition moments ($\alpha = 0$) using two-photon excitation, $r_0^{(2)} = \frac{4}{7} = 0.571$.

2 Materials and methods

2.1 Cell culture

The human alveolar epithelial A549 cell line was routinely maintained in modified eagle's medium with glutamax (MEM, Gibco, Paisley, United Kingdom) supplemented with 10% non-heated inactivated foetal bovine serum (FBS, Biochrom AG, Berlin, Germany) and 1% penicillin/streptomycin (P/S, Gibco) at 37°C under 5% CO_2. The human cervical cancer HeLa cell line was maintained in Dulbecco's Modified Eagle's Medium (Sigma-Aldrich, Ayrshire, United Kingdom) supplemented with 10% FBS and 1% P/S at 37°C under 5% CO_2. The MRC-5 cell line, human foetal lung fibroblasts, was cultured in modified eagle's medium (MEM-Earles & L-Glutamine, Gibco, Paisley, United Kingdom), supplemented with 10% FBS and 1% P/S at 37°C under 5% CO_2. For routine passaging, cells were washed with versene (Gibco) and detached using 0.05% trypsin containing 0.02% EDTA (Sigma-Aldrich, Ayrshire, United Kingdom).

2.2 Transfection procedure

The transfection procedure was optimized in HeLa cells. Therefore commercial available plasmids pLifeAct-mTurquoise2 and pmTurquoise2-Tubulin (Addgene, Cambridge, United Kingdom) were used to obtain actin and tubulin labelled with mTurquoise2. This cyan label was chosen because of its high-fluorescence quantum yield, long mono-exponential fluorescence lifetime and photostability[(36)]. The plasmids were amplified in Escherichia Coli in bacterial Lennox LB agar (Sigma-Aldrich) and purified according to the protocol of the plasmid midi kit (Qiagen, Venlo, Netherlands). Finally, isolated plasmids were sequenced to verify the coding sequence. Therefore multiple primers were designed to be able to read the full sequence (Appendix section 6.2 – 6.3). Sequencing was performed at VIB Genetic Service Facility, University of Antwerp. Prior to the transfection, A549 cells were seeded in a µ-slide 8-well IbiTreat chamber (Ibidi, Munich, Germany) at a density of 20 000 cells/well and cultured with 200 µl MEM containing 10% FBS and 1% P/S at 37°C. The cells were kept under 5% CO_2 until reaching 70-90% confluence. Lipofectamine® 3000 (Invitrogen, Belgium) was used as transfection reagent together with P3000™ Reagent (Invitrogen) to improve the transfection efficiency. Further, transfection was performed according to the protocol of Lipofectamine® 3000. Liposomes were prepared by adding plasmid DNA (400 ng) diluted in serum-free medium to P3000™ reagent and Lipofectamine® 3000 (1 µl). Next cells were incubated with complexes for 4 hours at 37°C.

2.3 BaTiO3 nanoparticles

The $BaTiO_3$ NPs were obtained from two different sources. One part of the NPs was synthesized at the Inorganic and Physical Chemistry department of the Hasselt University (Diepenbeek, Belgium). Here, the solvothermal reaction protocol based on the work of Lee et al. at the Advanced Institute of Science and Technology, Korea was employed[15]. This method uses barium hydroxide monohydrate ($Ba(OH)_2 \cdot H_2O$) and titanium butoxide $Ti[O(CH_2)_3 \cdot CH_3]_4$ as starting materials. The other $BaTiO_3$ NPs were obtained from the Institute of Condensed Matter Chemistry of Bordeaux (ICMCB-CNRS-France). These NPs were produced using a single-step synthesis method under supercritical conditions. For this solvothermal process, water is used mostly as the supercritical fluid[37]. To avoid agglomeration in solution, NPs were functionalized with aminomethylphosphonic acid (AMPA) or with citric acid at pH 7. For the ease of communication, samples using NPs from the Chemistry department of Hasselt University will be labelled “Lee” and samples using NPs from ICMCB-CNRS Bordeaux will be labelled “France”.

2.3.1 Characterization of NPs

For the characterization of the NPs dynamic light scattering (DLS), zeta potential and transmission electron microscopy (TEM), were employed. Using DLS, particle diameter and dispersity could be analysed. DLS measurements were obtained using a ZetaPals Zeta potential analyze (Brookhaven Instruments Corporation, New York, USA). The TEM images were recorded with the instrumentation of the Institute of Materials Research of the University of Hasselt (Diepenbeek, Belgium).

2.3.2 Cytotoxicity

Potential toxic effects of $BaTiO_3$ on living cells were studied using a cell viability assay. A549 cells were seeded in a 96-well plate at 5 000 cells per well, one day before treatment. The cells were treated with $BaTiO_3$ NPs dissolved in complete growth medium (concentrations ranging from 48 to 288 µg/ml) and ultrasonicated for one hour. After treatment of 24 hrs at 37°C/5% CO_2, the number of viable cells was determined using the CellTiter 96® Aqueous One Solution Cell Proliferation Assay (Promega, USA). Absorbance was read at 490 nm using Fluostar Optima microplate reader (BMG Labtech, Germany).

2.4 A549 exposure to $BaTiO_3$

Prior to exposure, cells were seeded in a µ-slide 8-well IbiTreat chamber (Ibidi, Munich, Germany) at a density of 20 000 cells/well. After 24 hrs incubation, 50 µg $BaTiO_3$ was added to each dish. Therefore $BaTiO_3$ stock solution was diluted in growth medium (MEM) and ultrasonicated for 1 h. During the exposure, cells were maintained 4 or 24 hrs at 37°C at 5% CO_2. To examine the role of the tubulin network in cellular dynamics, cells were exposed to

25 µM nocodazole (Sigma-Aldrich, United Kingdom), a microtubule-disrupting agent, for 1 h.[38]

2.5 Immunocytochemistry

Prior to the experiments, A549 cells were seeded on 12 mm glass coverslips (Menzel-Gläser, Germany) at a density of 50 000 cells per coverslip. For immunostaining, the cells were fixed in 4% formalin (Sigma-Aldrich) in sterile phosphate-buffered saline (PBS) for 15 min at 37°C. Next the cells were washed with PBS and permeabilized with 0.5% Tween 20 in PBS for 10 min. The permeabilization was stopped by rinsing the cells with 0.1% Tween 20 in PBS and by adding blocking buffer (0.1% Tween 20 and 2% BSA dissolved in PBS) for 30 min. The cells were incubated with the primary monoclonal (DM1A) mouse anti-α-tubulin antibody (Sigma-Aldrich) in blocking buffer (1:1000) for 30 min. After rinsing with PBS-0.1% Tween 20, the incubation with secondary Alexa Fluor® 488 donkey anti-mouse IgG (Life Technologies, Belgium) in blocking buffer (1:250) was performed for 30 min. Simultaneously, the high-affinity F-actin probe Alexa Fluor® 647 phalloidin (Life Technologies, Belgium) was incubated. To mount the cells on a glass coverslip, Immu-Mount (Thermo Scientific, Waltham, USA) was used. Cells were observed with confocal laser scanning microscope as described in the next section.

2.6 Microscope instrumentation

Imaging experiments were performed in an air-conditioned room with a constant temperature (19°C). The equipment was placed on a vibration-isolating table to minimize errors. For the imaging an epifluorescence Axiovert 200M with a Zeiss LSM 510 Meta confocal laser scanhead (Zeiss, Jena, Germany) was used in combination with a LD C-Apochromat 40x/1.1 W Korr UV-VIS-IR objective from Zeiss. Excitation light was sent through a main dichroic beam splitter (HFT 488), a secondary beam splitter (NFT 490) and a band-pass emission filter (500-550) before going to the photomultiplier tube (PMT) from Hamamatsu (Mont-Saint-guibert, Belgium). The transfected cells were excited using a 150 fs pulsed laser light of a two photon Ti:Sapphire laser (MaiTai, Spectra-Physics, Santa Clara, USA) tuned at an output wavelength of 820 nm. The emission light was detected using non-descanned detection: the fluorescence was directed using a short-pass (KP) 685 and a BP 400-410 towards a PMT. In the live cell imaging experiments, the cells were kept at 37°C by the means of a small stage incubator (Pecon, Erbach, Germany). For excitation of the Alexa Fluor® 488 the Argon-Ion laser with an excitation line of 488 nm was used and for the Alexa fluor® 647 the Helium-Neon laser with an excitation line of 633nm was used. To test the SHG-activity of the $BaTiO_3$ NPs, sample were excited using a 150 fs pulsed laser light of a

two photon Ti:Sapphire laser (MaiTai, Spectra-Physics, Santa Clara, USA) tuned at an output wavelength of 810 nm. Fluorescence anisotropy experiments were performed on a modified image set-up. Analogue detectors were replaced by the H7422 series detectors from Hamamatsu (Mont-Saint-guibert, Belgium). A time-correlated single photon counting (TCSPC) module (SPC-830) from Becker & Hickl GmbH (Berlin, Germany) was used to perform fluorescence lifetime measurements. Moreover, a polarizer was added to the excitation side of the light path to obtain polarised light. Finally, a polarized beam splitter is placed at the emission side to separate horizontally from vertically polarized emission light.

2.7 Image correlation spectroscopy

All ICS techniques are based on the intensity fluctuation analyses of an image or a stack of images[39]. Furthermore they all require the calculation of an autocorrelation function (ACF), either in the temporal domain, in the spatial domain or both. Most ICS-analogues use a time-series in three dimensions: the *XY* plane and time *T*. Therefore the resulting time-series is denoted as $i(x,y,t)$ describing the intensity fluctuation for a pixel at location (x,y) in the image detected at time t.

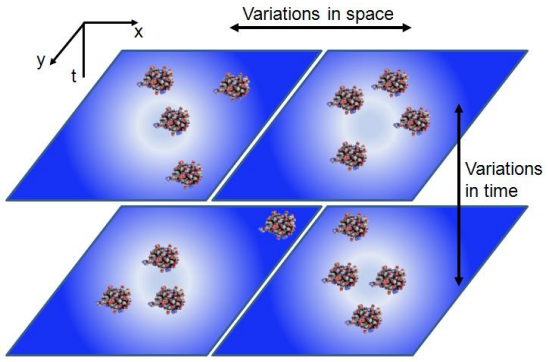

Figure 4: Molecular variations in space and time within the point spread function (PSF)
(Based on figure 10.2 Wiseman, P.W., Methods in Enzymology[27])

To correlate fluorescence fluctuations over time, space or both, all ICS analogues rely on the convolution of the microscope point spread function (PSF) with the point-source emission from the fluorophores due to diffraction. Each frame of the recorded time-series can be represented by such a convolution[40]. Knowing that i depends on three variables, an intensity fluctuation δi can be defined[27, 39]:

$$\delta i(x,y,t) = i(x,y,t) - \langle i(x,y,t)\rangle_T \qquad (9)$$

The $\langle \ldots \rangle$ brackets represent the intensity average between images from a time series stack[27] $\delta i(x,y,t)$ is the spatiotemporal intensity fluctuation around the ensemble average and $\langle i(x,y,t)\rangle_T$ represents an image with resolution XY that holds for each pixel the time average for that pixel position throughout the stack of images.[39]

2.7.1 Spatiotemporal image correlation spectroscopy (STICS)

This technique is an extension of ICS and ICCS and its goal is to obtain information about the direction of the particles exiting the correlation areas when flux is present and to obtain flow vectors. STICS entails the analysis of spatial fluctuations around the mean fluorescence intensity within a time series of *t* images by calculating the spatial autocorrelation function (SACF)[26]. The SACF is a special case of the spatiotemporal autocorrelation function (STACF) because of the zero time lags and of the absence of averaging over the stack of *t* images.

The spatiotemporal autocorrelation function is given by:

$$g(\xi,\eta,\tau) = \frac{\langle \delta i(x,y,t)\delta i(x+\xi, y+\eta, t+\tau)\rangle}{\langle i(t)\rangle_{x,y}\langle i(t+\tau)\rangle_{x,y}} \quad (10)$$

Spatial correlation function:

$$g(\xi,\eta) = \frac{\langle \delta i(x,y,t)\delta i(x+\xi, y+\eta)\rangle}{\langle i(t)\rangle_{x,y}{}^2} \quad (11)$$

The output obtained after a STICS analysis is a spatiotemporal correlation function stack. This one space-time autocorrelation function contains information about the time evolution of the spatial correlations of the fluorophores in the detection volume. These spatial fluctuations are defined by the underlying molecular dynamics and the emission photo physics[27].

At time lag zero $(\tau = 0)$ each image will be correlated in space with itself. The outcome is a correlation function with a maximum at zero spatial lags. This function decays as a three dimensional Gaussian due to the spatial profile of the point spread function[27]. From this 3D Gaussian peak, flow vectors can be calculated and information about the transport dynamics can be obtained. When stationary particles are present, the correlation peak is centred at $(\xi = 0, \eta = 0)$ and remains unchanged at different time-lags τ. Dynamics of the particles cause the correlation peak to change. Diffusing particles cause the correlation peak to broaden because they tend to leave the correlation area. Therefore $g(\xi,\eta,\tau)$ decays in amplitude and spreads radially over time τ. In the case of directed flow, the amplitude of the peaks stays unchanged, but instead its centre is shifted $(\xi = -v_x \times \tau;\ \eta = -v_y \times \tau)$. From this movement flow vectors, describing the direction of flow, can be drawn[41]. With the zero-lags amplitude $g(0,0,0)$, the longtime offset r_∞ and ω_0 as fit parameters, the spatial autocorrelation portion can be fit by nonlinear least squares with a 2D Gaussian function[40, 42]:

$$g(0,0,0) = g(0,0,0)exp\left(-\frac{\xi^2+\eta^2}{\omega_0^2}\right) + r_\infty \quad (12)$$

Because cells are heterogeneous diffusion, flow and immobile populations will be present simultaneously.

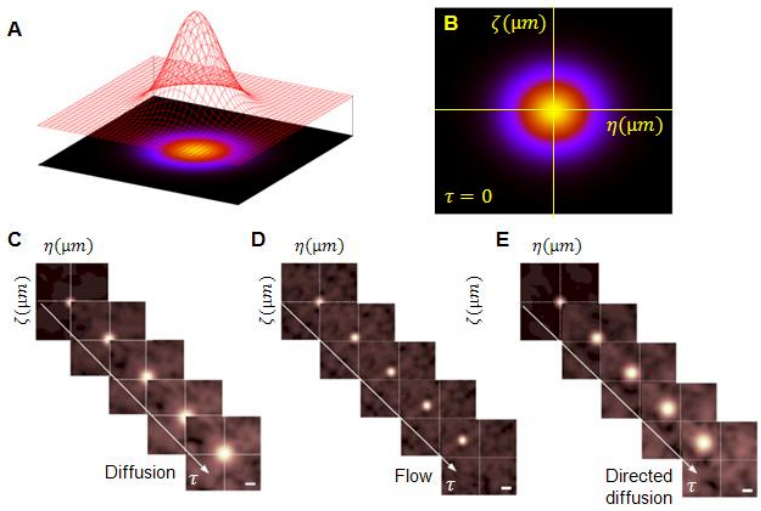

Figure 5: Spatiotemporal image correlation spectroscopy (STICS). (A) *Spatiotemporal autocorrelation function (STACF) at time lag zero.* ***(B)*** *Top view of the Gaussian STACF from* ***(A)****.* ***(C-E)*** *Plots (top view) of STACF as function of time. The particles undergo diffusion, flow and directed diffusion respectively. (Based on figure 10.4 Wiseman, P.W., Methods in Enzymology[27])*

The static or slowly moving populations can impede the correlation fitting and needs to be removed. For this reason a Fourier-filtering is used before starting the correlation analysis. This "immobile filter" eliminates the immobile population contribution by filtering of the minimum frequency component for every pixel trace in time. For a given pixel trace, the contributions of the dynamic processes in the fluorescence fluctuations change as a function of time. However the immobile population provides an intensity offset, constant in time, to the single pixel intensity. Hence eliminating the minimum frequency component removes the immobile component contribution. The intensity correction carried out for each pixel location (x,y) is given by[27, 42]:

$$i'_a(x,y,t) = F_f^{-1}\left\{F_t\{i_a(x,y,t)\} \times H_{1/T}(f)\right\} \tag{13}$$

Here T represents the total acquisition time of the image series, $H_{1/T}(f)$ reflects the Heavyside function which is 0 for f < 1/T and 1 for f > 1/T. The inverse Fourier-transform is given by F_i^{-1} with respect to variable *i* and f as the pixel temporal-frequency variable.

2.7.2 Spatiotemporal image cross-correlation spectroscopy

As with STICS, an autocorrelation function needs to be calculated. For a collection time *t*, the normalized spatial intensity fluctuation autocorrelation function, with detection channel $a = b = 1$ can be defined as previously seen, Eq. (10). When defining a cross-correlation function $a \neq b$ (e.g.: $a = NPs; b = lysotracker$), the autocorrelation function is therefore defined by[43]:

$$g_{ab}(\xi,\eta,\tau) = \frac{\langle \delta i_a(x,y,t)\delta i_b(x+\xi, y+\eta, t+\tau)\rangle}{\langle i_a\rangle_t \langle i_b\rangle_{t+\tau}} \tag{14}$$

For these experiments, cells were exposed to $BaTiO_3$ - Lee NPs for 24 hrs and lysosomes were labelled with Lysotracker Green (Invitrogen) preceding the imaging. Cells were incubated with Lysotracker Green (1 μM) for 30 min. at 37°C and 5%. Imaging was performed using the setup described earlier and for each cell a time-series of 100 frames was collected.

2.7.3 Temporal image correlation spectroscopy

When the time correlation function is defined, both transport mode and rate of the particles are demonstrated. In TICS it is important that the imaging rate is appropriately matched to the time scale of the process of interest. Otherwise it is not possible to provide correct measurements. From a temporal autocorrelation function, there are generally three parameters of interest: the amplitude (which is inversely proportional to the number of particles), the decay shape (which determines the mode of transport, e.g. diffusion or flow) and the rate of decay (which describes how fast the dynamic process is occurring)[40]. A temporal intensity fluctuation correlation function can be seen as a spatiotemporal correlation function with zero spatial lags:

$$g(0,0,\tau) = \frac{\langle \delta i(x,y,t)\delta i(x,y,t+\tau)\rangle}{\langle i(t)\rangle\langle i(t+\tau)\rangle} \quad (15)$$

Eq. (15) is simply Eq. (10) evaluated with zero spatial lags and can be seen as the temporal reiteration of the average spatial correlation between the time series images separated by a time delay τ[43]. An important remark has to be made: because only time is used as a variable, nothing is known about locations. Therefore it is not possible to determine the direction of the flow[41].

Dynamic processes influence the temporal fluorescence fluctuations and therefore the decay of the correlation functions. For specific cases of two-dimensional transport phenomena (flow and diffusion), analytical solutions for the generalized intensity fluctuation correlation function are needed. Four such functional forms can be considered: for two-dimensional diffusion, for two dimensional flow, for two-dimensional diffusion and flow in a single population, and for two dimensional diffusion and flow for two populations[24]. Complete equations for each model are given in the Appendix, section 6.4. During analysis, the temporal autocorrelation function $g(0,0,\tau)$ is fitted against all four analytical decay models. The best-fitted model is then used for the determination of the diffusion coefficients.

2.8 Procedures of image data analysis

To perform the image data analysis, custom written MATLAB (The Mathworks, Eindhoven, The Netherlands) routines were used, based on the work of Wiseman Research Group, McGill University[40, 42, 44]. Prior to the STICS analysis, slowly moving or immobile fractions,

influencing the Gaussian correlation were removed by Fourier-filtering[40, 42]. Next the STACF for sub-regions of 64x64 pixels of the images was calculated using Eq. (10). The same sub-regions are used for calculating the TICS temporal autocorrelation functions by Eq. (15). Because the STACF has a higher power to determine the flow velocity, the values analysed with STICS were used in Eq. (A.3) to obtain the best fit for the TACF. Diffusion coefficients were measured by using the best-fit characteristic diffusion time and $\omega_{0.}$ The latter was acquired by averaging the individual ω_0 obtained by fitting Eq. (12). To correct for cell movement and motion of the stage, STICS analysis was performed on the whole cell for each individual cell.

2.9 Anisotropy measurements

As in this study fluorescence anisotropy is implemented in the setup for the first time, validation tests needed to be performed. First rhodamine 6G (R6G) was dissolved in a serial dilution of glycerol (0, 50, 60, 70, 80 and 100 v/v%) to test the technical adjustments. Subsequent, artefacts caused by the system were analysed. Because detectors are removable, effects arising from rotation of the detector needed to be considered. Furthermore influences from the dichroic mirror reflecting emission light to the detection system were examined. Therefore a smaller, separate setup consisting of a laser (Laserhead HeNe 633-5P, Qioptiq Photonics, Munich, Germany), a polarizer (Glan-Thompson, UK) and a photo-diode was used. To correct for the difference in sensitivity between both detectors the G-factor is determined. Therefore decay curves of R6G in glycerol and water were measured using circularly polarized light. In this case both detectors should analyse exactly the same intensities. Finally the instrument response function (IRF) of the confocal system was measured, using potassium hydrogen phosphate (KDP) crystals generating strong SHG signals. Therefore KDP is dissolved in water, a small droplet is placed on a cover slip and dried. Polymers loaded with fluorescein (CEIB, University of Liège, Belgium) are used to test anisotropy. Information about the polymers is limited because of their confidential nature. Fluorescein is attached to the polymer via an ester linkage, the latter being a target of the hydrolase enzyme esterase. Adding these polymers to cells possibly causes the ester-linkage to be cleaved and the fluorescein to move freely. To evaluate cleavage has occurred, data are compared with data from cells exposed to free label. For these experiments MRC-5 cells were seeded in µ-slide 8-well IbiTreat chamber (Ibidi, Munich, Germany) at a density of 15 000 cells/well and exposed to the polymers (10 µM) for 24 hrs. The data consists out of two time resolved curves, analysed globally. In other words, both curves are analysed simultaneously by linking the common parameters in the fitting functions. Calculations were performed using custom written MATLAB routines.

3 Results & Discussion

3.1 Characterization of BaTiO3 NPs

A comprehensive characterization of the physicochemical properties of the NPs was carried out. To verify the dimensions of the $BaTiO_3$ NPs used in this study, TEM and DLS analysis were performed. Dispersion characteristics and size distributions were studied by means transmission electron microscopy (TEM), dynamic light scattering (DLS) and zeta potential (ζ-potential).

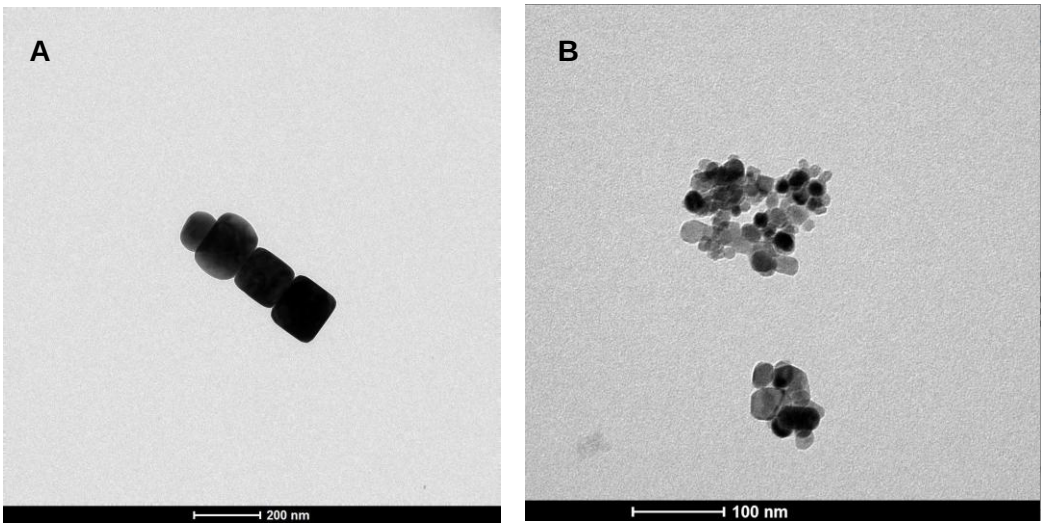

Figure 6: TEM images of $BaTiO_3$ NPs. *Particles presented in **(A)** are synthesized recording to Lee et al. in part **(B)** are obtained from ICMCB-CNRS-France. The images show the nano-sized diameter of the NPs: 80 nm **(A)** and 20 nm **(B)***

TEM images approve the diameter of the unfunctionalized $BaTiO_3$ – Lee NPs to be approximately 100 nm and that the NPs from Bordeaux have a diameter of around 20 nm (*figure 6)*. DLS data show the diameter range of the NPs functionalized with AMPA (*figure 7)*. A small increase in diameter of the $BaTiO_3$ – Lee NPs functionalized with AMPA (~170 nm) in comparison with the non-functionalized NPs (~100nm) can be seen. The increase of diameter with increasing concentration of NPs in solution is probably a consequence of agglomeration. In this study, NPs were used in combination with live cells. Therefore, NPs were dissolved in complete growth medium, a solvent different from their original stock dispersion. For this reason, DLS measurements were repeated using functionalized NPs dissolved in complete growth medium.

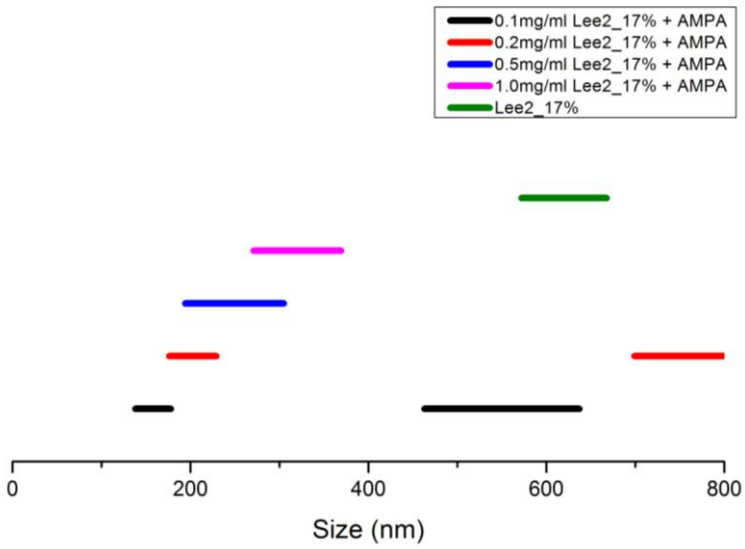

Figure 7: DLS data revealing the diameter range of the NPs functionalized with AMPA.

Dispersing NPs in biological fluids, such as complete growth medium, causes their physicochemical properties to change[45]. Since a lot of proteins are present in culture medium, protein-NP interactions will lead to formation of a protein corona around the NPs, influencing live cell experiments. Performed DLS measurements of NPs dissolved in culture medium reveal a large increase in diameter. Since the values are fluctuating strongly, and large standard deviations are seen, they were not reproducible. Therefore no data are presented. Moreover, because of aggregation and sedimentation of the unstable NP-dispersion, the data demonstrate the dimensions and polydispersity of the clustered NPs or from the proteins present in the growth medium, rather than from single NPs. Consequently, no solid conclusions can be drawn about the properties of the NPs in culture medium.

Next there is the problem of the duration of the DLS analysis. As described by Maiorano et al. (2010), hydrodynamic radii of NPs dissolved in growth medium are increasing slowly until reaching a stable phase after more than 24 hrs[45]. During the short time-period of the experiments described earlier, the evolution of the hydrodynamic radii was not yet stabilized causing the fluctuations. To get stable results, representing the hydrodynamic radius of the NPs dissolved in growth medium, DLS measurements over time (> 24 hrs) need to be employed.

The zeta potential is an indicator for the stability of the NPs in solution. Aggregation of particles will be prevented if they carry an equal charge and a high zeta potential. Therefore stability of the dispersion is created by the repulsion generated by the charged NPs. To analyse the stability of the NPs dispersed in complete growth medium, zeta potentials of different NPs are measured. Previous studies have demonstrated decreasing zeta potentials of functionalized $BaTiO_3$ with respect to untreated NPs, possessing values of approximately -

20 mV[46]. The zeta potentials obtained in the present study are fluctuating strongly between different measurements. As in the case of DLS, protein coatings change the intrinsic properties of the NPs, thereby altering the zeta potentials to more negative values[45]. Since these experiments are performed on the same time-scale as DLS and the same issues are underlying the fluctuating values, the data were not reproducible and are therefore not presented. Furthermore, it is difficult to distinguish whether the charge is measured at the protein corona or at the hydrodynamic radius. Therefore, using the obtained values makes it difficult to draw scientific reliable conclusions. Repeating the experiments with a more stable dispersion and for a longer period of time will yield stable and more reliable results.

3.2 Effect of BaTiO3 NPs on cell viability

When the intracellular behaviour of the NPs is studied, toxic effects should be considered. To exclude adverse effects of $BaTiO_3$ NPs on cells, influencing the dynamics experiments, cell viability assays were performed. From these assays, percentage of viable cells after treatment of 24 hrs with NPs was obtained (*figure 8*). During testing, $ZnSO_4$ (15 µg/ml) was used to induce cell death, serving as a negative control[47]. Incubating cells for 24 hrs with NPs functionalized with AMPA (288 µg/ml for $BaTiO_3$ – Lee and 700 µg/ml for $BaTiO_3$ – France) causes little adverse effects on cell viability. However, the majority of the cells (>69%) is still unaffected after exposure (*figure 8A*). Noticeable is the difference in viability between $BaTiO_3$ - Lee and $BaTiO_3$ – France functionalized with citric acid. The latter exert less toxicity to the cells, while one expected these smaller NPs to penetrate more easily and interfere with cellular processes. Yet, the same diameter-dependent effect is ascertained by Faust et al. (2014), showing apoptosis is more rapidly induced by larger NPs via production of reactive oxygen species (ROS)[48]. In this study, the human placental cell line BeWo b30 was grown as epithelia and exposed to iron oxide (α-Fe_2O_3) NPs. Subsequently, ROS production was determined using the fluorescence of of 2′,7′-dicholorofluorescein. Cell viability was analysed using the ethidium homodimer-1, which intercalates into DNA upon nuclear-membrane disruption. After intercalation, fluorescence of ethidium increases strongly, which can be measured using a fluorescence microscope. By escaping endosomes, iron oxide NPs are able to elicit ROS production and rupture of the lysosomes. Combined with an increased expression of pro-apoptotic genes, this contributes to cell death of the apoptosis variety. The same study of ROS production can possibly applied to the $BaTiO_3$ NPs. Together with cell viability assays for long-term exposure, this may reveal new comprehensions into the toxicity of NPs.

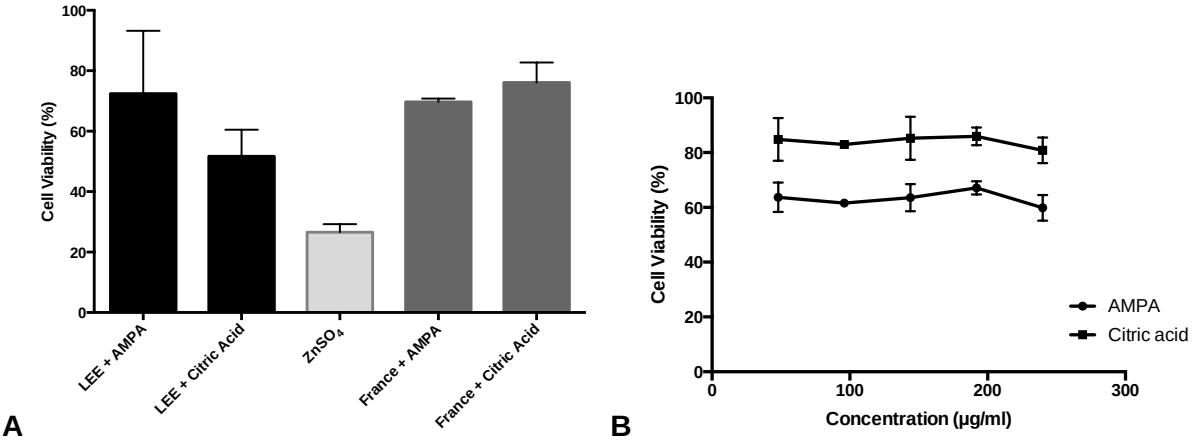

Figure 8: Percentage of viable cells after treatment with $BaTiO_3$ NPs. *Percentage of viable A549 cells determined with CellTiter 96® Aqueous One Solution Cell Proliferation Assay after 24 hrs treatment with $BaTiO_3$ NPs at different concentrations:* ***(A)*** *Concentration used: 288 µg/ml ($BaTiO_3$ - LEE) and 700 µg/ml ($BaTiO_3$ - France), $ZnSO_4$: 15 µg/ml* ***(B)*** *Dose-response curves of A549 cells exposed to $BaTiO_3$ - Lee NPs to examine concentration-related effects. Error bars represent the standard deviation of the three replicates.*

By exposing A549 cells to different concentrations of $BaTiO_3$ – Lee NPs, ranging from 48 to 240 µg/ml, a dose-response relation was constructed (*figure 8B*). Increasing the concentration of $BaTiO_3$ does not translate in to large differences in cell viability. Probably the range of concentrations used for this experiments was not wide enough, explaining the quasi-horizontal curve. However, because from toxicological point of view, high concentrations were used, the NPs can be said to be have minor cytotoxicity.

3.3 Labelling actin and tubulin structures with mturquoise2 using plasmids

As mentioned above, cytoskeletal structures, such as the microtubules, play a prominent role in cellular transport of molecules. Their structures serve as moving tracks for intracellular transport, accomplished by motor proteins 'walking' along these structures[(49)]. Previous research has demonstrated the ability to study the movement of NPs along tubulin structures and has found that endocytic vesicles and NPs are transported along the tubulin tracks [(50)]. Therefore, tubulin structures were labelled via transfection to study the contribution of the tubulin network to intracellular transport of $BaTiO_3$ NPs. In co-localization experiments, the fluorescent images could function as a 'mask' to exclude particles not present at the location of the structures and to use for correlation analysis. These data can subsequently be used to study the movement of the NPs along these structures together with the contribution of motor proteins. Moreover, this method can be used in exclusion studies to study the involvement of different cellular structures to the intracellular uptake and transport of NPs.

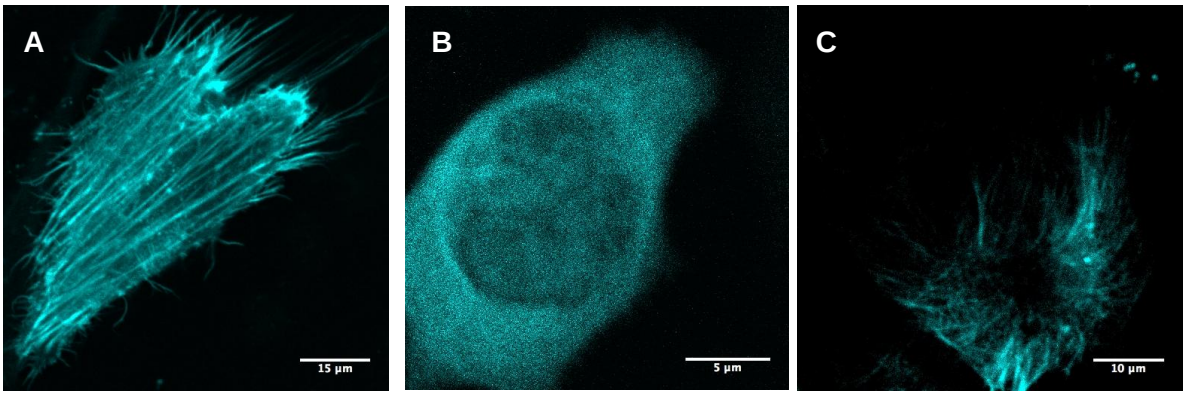

Figure 9: HeLa cells expressing mTurquoise2 fused to actin and to tubulin. *Using the method of transfection, the cyan label mturquoise2 is fused to actin* ***(A)*** *and tubulin structures* ***(B+C)****. Because of over-expression and poor localization, Paclitaxel is added after transfection with the pmTurquoise2-Tubulin plasmid* ***(C)****.*

Fluorescence microscopy images of HeLa cells transfected with mTurquoise2 reveal the expression of actin and tubulin structures labelled with mTurquoise2 (*figure 9*). In contrast to tubulin, labelling of actin structures using the transfection protocol works well (*figure 9A*). The pmTurquoise2-Tubulin construct does not localize very well due to over-expression. Therefore the tubulin network is sometimes rarely visible. To improve the localization Paclitaxel was added (1 h) to stabilize the polymerized tubulin-network, making the microtubules more visible. Paclitaxel is an antineoplastic agent used as an anti-cancer drug. It stabilizes and promotes microtubule assembly by non-covalent interaction with tubulin, thereby inhibiting cellular growth[51]. In research Paclitaxel is used as a microtubule stabilizer. It stabilizes the tubulin polymer, maintains microtubule integrity and protects them from disassembly[52]. Therefore paclitaxel has a positive effect on the tubulin transfection: the tubulin network is coming more visible, yet still less clear than actin filaments. Because an effect of Paclitaxel on the dynamics of NPs cannot be excluded, care has to be taken when using this agent. Prior to transfection, plasmids were amplified in E. Coli and purified using a plasmid midi kit. To verify mal-expression of the labelled tubulin is not caused by errors in the coding nucleotide sequence, these plasmids are sequenced following the Sanger method. The outcome of the sequencing (Appendix section 6.3) was aligned with the sequence of the developer using the Basic Local Alignment Search Tool (BLAST) of the National Centre for Biotechnology Information (NCBI). The alignment analysis does not reveal errors underlying the expression issue.

3.4 Study of cytoskeleton and the effect of inhibiting agents using immunocytochemistry

Immunostaining of A549 cells reveals the actin filaments and the tubulin network (*figure 10 + 11).* Actin filaments (F-actin) are present as longitudinal structures, scaffolding the cell and providing routes for intracellular transport[53, 54]. To examine the role of tubulin in intracellular transport, nocodazole, an anti-microtubule agent is added to the cells exposed to NPs.

Preceding the experiments, the working concentration of nocodazole was optimized. Based on the literature, a concentration range (15, 20 and 25 µM) was used to obtain an optimum (*figure 10*)[55]. These experiments demonstrate 25 µM to be an ideal working concentration.

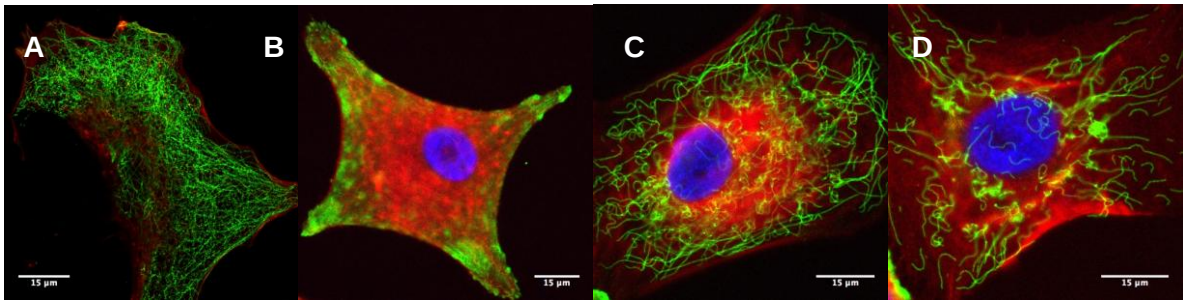

Figure 10: Effect of Nocodazole an the tubulin network of A549 cells*. To find a, optimal working concentration, A549 cells were treated with 15 µM* ***(B)****, 20 µM* ***(C)*** *and 25 µM* ***(D)*** *respectively. Via immunostaining the tubulin network (green), F-actin (red) and the nucleus (Blue) the effects of the different concentrations are studied compared to control cells* ***(A)****. The highest concentration (25 µM) gives the best outcome, and is therefore used in further experiments. Scale bar is 15 µm.*

In order to examine the effect of nocodazole, A549 cells were fixed and immunostained after treatment with the depolymerizing drug. From the confocal images, the tubulin network and actin filaments can be distinguished. Moreover SHG signals from the $BaTiO_3$ NPs can be detected.

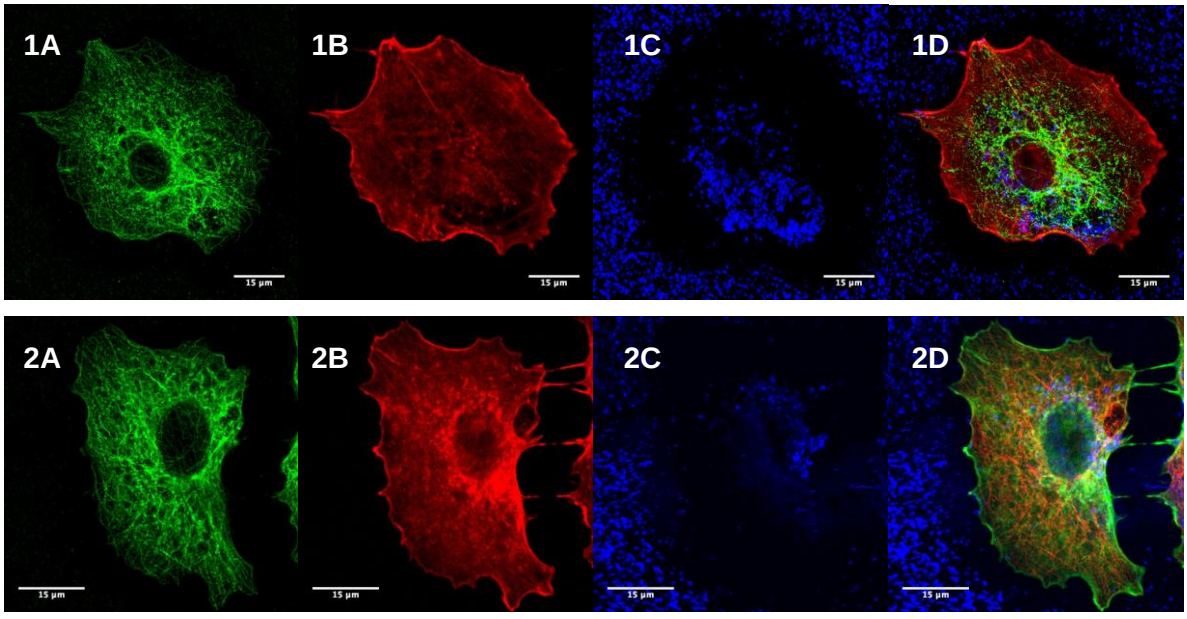

Figure 11: Stained tubulin network and actin filaments of an A549 cell exposed to $BaTiO_3$ – France NPs. *By immunostaining the A549 cells exposed to French $BaTiO_3$ functionalized with AMPA* ***(1)*** *or citric acid* ***(2)****, the tubulin network* ***(A)*** *and F-actin* ***(B)*** *is visualized. At the same time the SHG activity of the NPs can be detected* ***(C)****.* ***(D)*** *demonstrates the overlay of the three channels. Scale bar is 15 µm.*

The effect of nocodazole on the polymerization of microtubules can be clearly shown using immunocytochemistry (*figure 10*). Before treatment, a network of longitudinal tubulin structures is clearly present, meaning polymerization is successful full-filled. On the other hand, nocodazole prevents this network from being formed by interrupting the polymerization

process. Hence tubulin monomers accumulate in the cells and no linear structures are visible. This means a serious shrinkage in cellular scaffolding and intracellular dynamics.

3.5 Dynamics of NPs elucidated by STICS and TICS

Several variants of ICS are carried out to study the dynamics of $BaTiO_3$ NPs in human cancer cells. This is because the effect of NPs on live cells is still unclear and not much is known about the dynamics of NPs in living systems. Flow and diffusional movement of NPs through living cells is analysed using TICS and STICS. These spectroscopy techniques reveal information about the phenomena of non-directed and possible directed motion of $BaTiO_3$ NPs through human A549 cancer cells. After recording image time-series of individual cells, different image subsections of 64x64 pixels (*figures 12C, 14A and 14B*) were selected to perform STICS and TICS analyses. When immobile fractions are removed, the STACF $g(\xi,\eta,\tau)$ for τ = 1, 20 and 40 s was calculated for each typical region (*figure 12A + B*). Moreover information regarding the peak position of $g(\xi,\eta,\tau)$ as a function of time was extracted from the analysis, which gives the direction and magnitude of flow (*figure 12D*). The Gaussian autocorrelation peak moves away from the centre as a function of time. Additionally, broadening of the peak indicates diffusion-biased flow. Since STICS analysis is more accurate, magnitude and direction of flow is calculated based on the STACF: fitting for the displacement of the Gaussian peak for the selected region in figure 12 yields a velocity V_{STICS} of $2.38\text{x}10^{-2}$ µm/s ($v_x = -2.29\text{x}10^{-2}$; $v_y = -4.31\text{x}10^{-3}$ µm/s). On the other hand, to obtain the diffusion coefficients four different models of TICS were used as explained in the section 2.7. As can be seen from figure 13 the TACF $g(0,0,\tau)$ is fitted well using Eq. (A.3) describing flow and diffusion for one population simultaneously. In TICS analysis, the fixed flow values obtained from the STICS analysis are used. Fitting TICS to TACF $g(0,0,\tau)$ yields a diffusion coefficient (D_{TICS}) of $(1.93\pm0.21)\text{x}10^{-3}$ µm^2/s for the selected region. The TICS and STICS analyses described earlier are applied to multiple cells for each condition. Analysing one cell consists of correcting for stage drift and cell movement, and selecting different regions of 64x64 pixels, as explained earlier. For each region the diffusion coefficient and magnitude of flow velocity is estimated using STICS and TICS analysis (*table 1*). As shown in the example above, the STACF is used for calculating flow velocity. The obtained value is used in TICS analysis for the study of diffusion coefficients using different decay models.

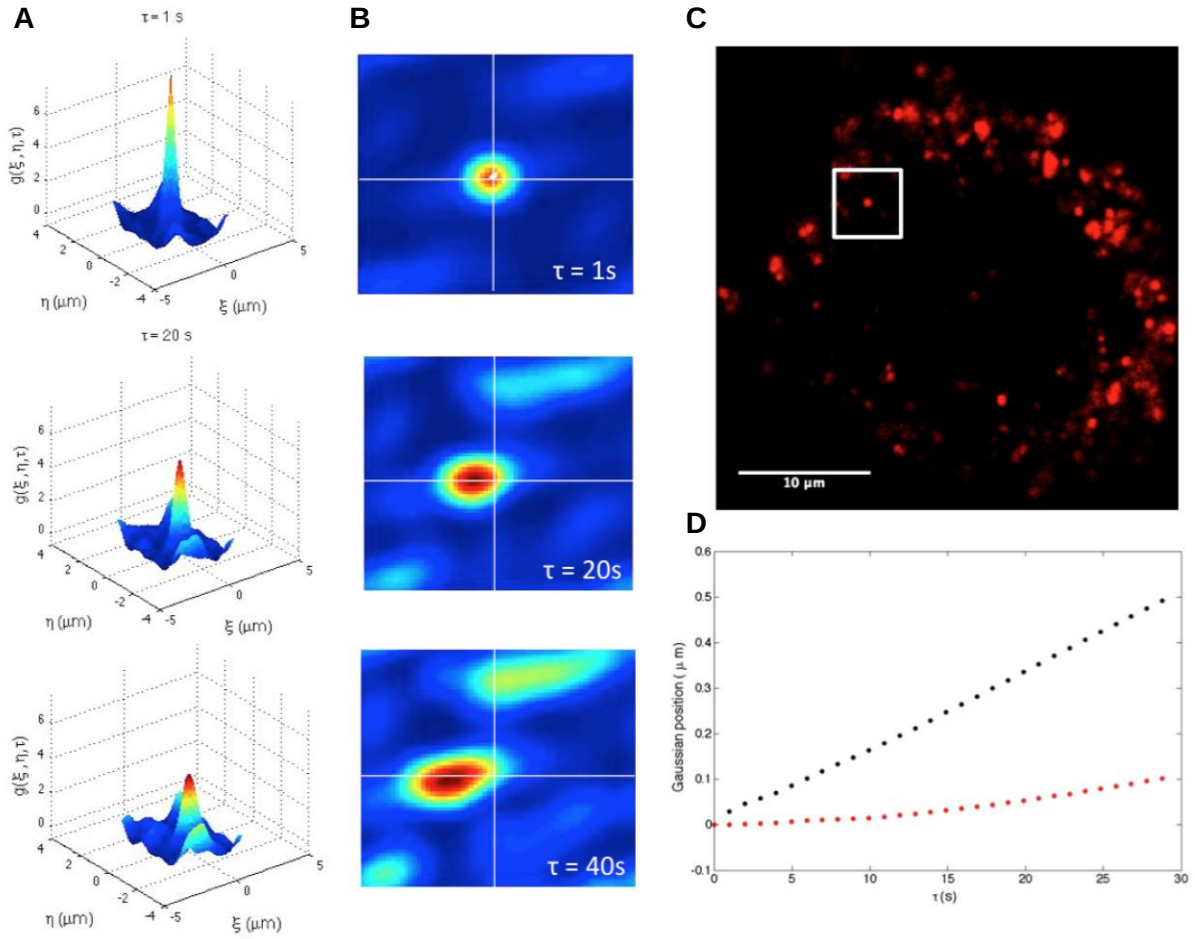

Figure 12: STICS analysis of a typical 64x64 pixels region of an A549 cell exposed for 4hrs to $BaTiO_3$ – France NPs functionalized with AMPA. *For the selected region* ***(C)*** *the Gaussian autocorrelation functions* $g(\boldsymbol{\xi},\boldsymbol{\eta},\boldsymbol{\tau})$ *and their contour plot* ***(B)*** *after removal of immobile fraction are presented. For STICS and TICS analysis, 200 frames were collected without any time delay between sequential images.* ***(D)*** *Position of the* $\boldsymbol{g(\xi,\eta,\tau)}$ *peak as a function of time. Based on the peak position in time, the concerted velocity of the particles (2.38x10^{-2} μm/s) can be calculated.*

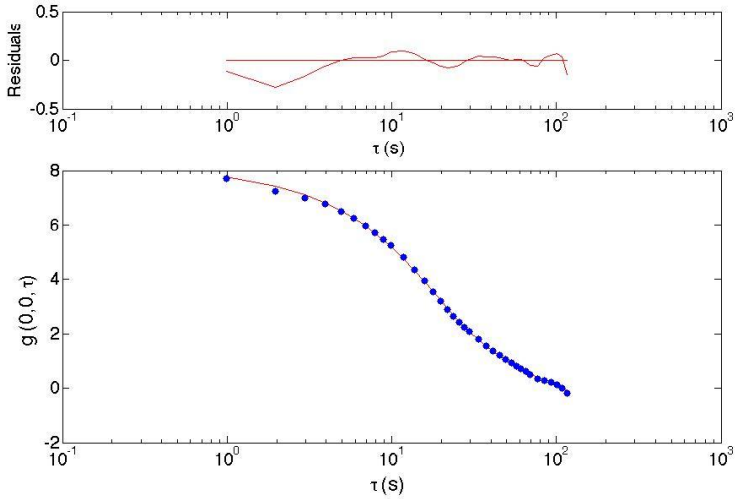

Figure 13: Fit of TICS to temporal autocorrelation peak $\boldsymbol{g(0,0,\tau)}$. *Based on the fit, an estimation of the particles diffusion coefficient (D_{TICS}) can be made: D_{TICS} = (1.93±0.21)x10^{-3} μm^2/s*

For each cell, these analyses were performed for ten selected regions. For each condition three cells were recorded and analysed. An overview is given in summarizing table 2. In order to use a normal mean and standard deviation, the data has to be well modelled by a normal distribution. Since this is not applicable for all data sets, geometric mean of the lognormal distribution (GM) is used to demonstrate the central tendency. The lower and upper confidence intervals (LCI and UCI) are used as indication for the spread of the GM. For the interpretation of these results, some issues need to be considered. The diffusion coefficients determined as described earlier are diameter-dependent. Since the NP-dispersion is unstable and aggregation occurs rapidly, diffusion coefficients are calculated for clusters, rather than NPs. Even when evaluating the data of flow velocity, these issues need to be taken into account. Using STICS analysis, information about magnitude and direction of flow is obtained. Based on the position of the Gaussian autocorrelation peak two vectors can be drawn, describing the direction of the flow in x and y direction (f*igure 12D*). Because these vectors describe the displacement of the Gaussian peak over time, a magnitude of velocity for each vector can be defined, which is given by the length of the representing vector. Combining both vectors to one resultant yields the net magnitude and direction of flow by particles in the selected region. For each selected 64x64 pixels region, these vectors are calculated and drawn on the recorded image. Mapping vectors of flow velocity (*figure 14*) indicates that the $BaTiO_3$ NPs move randomly and with different magnitudes through the cells.

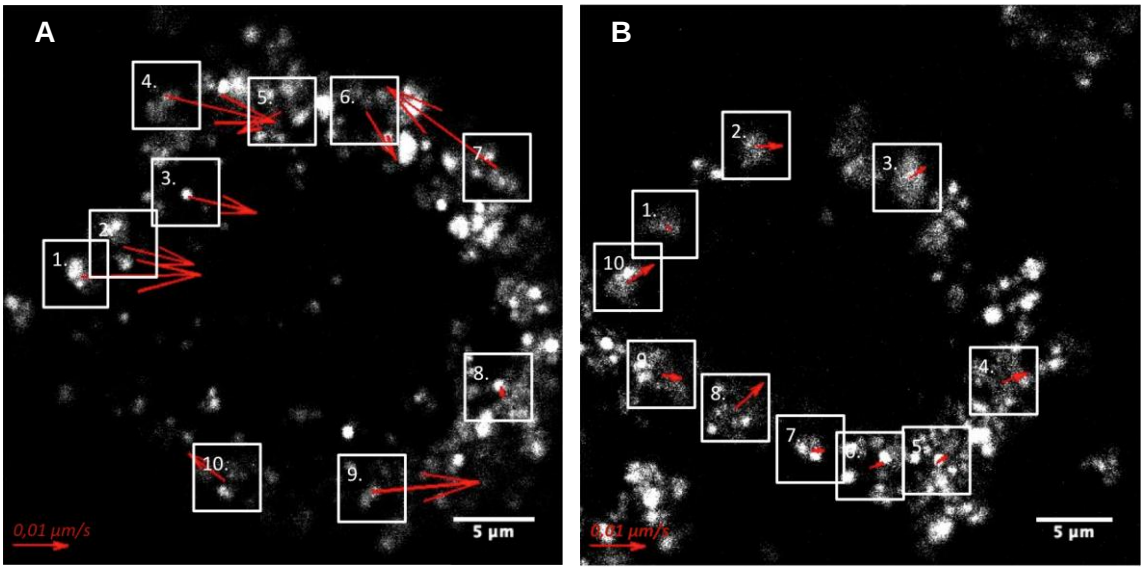

Figure 14: Map of velocity vectors of flow of $BaTiO_3$ – France NPs with AMPA. *Using the vectors in x and y direction obtained by STICS analysis, velocity vectors of flow are constructed for BaTiO3 – France NPs, before **(A)** and after **(B)** treatment with nocodazole.*

***Table 1: Diffusion coefficients and flow velocities for ten different regions inside A549 cells exposed for 4 or 24hrs to $BaTiO_3$ NPs**. For each condition, the influence of Nocodazole is tested. V_{STICS} is the magnitude of flow velocity calculated by STICS, using velocities in the $\boldsymbol{x}$ and $\boldsymbol{y}$ plane. During calculation, correction for stage drift and cell movement is done. D_{TICS} is the diffusion coefficient determined using TICS analysis. By fitting the TACF $\boldsymbol{g(0,0,\tau)}$ to four different models. The best-fitted model is used to calculate the diffusion coefficients.*

Regions	4hrs		4hrs + Nocodazole		24hrs		24hrs + Nocodazole	
	V_{STICS} (µm/s)	D_{TICS} (µm²/s)	V_{STICS} (µm/s)	D_{TICS} (µm²/s)	V_{STICS} (µm/s)	D_{TICS} (µm²/s)	V_{STICS} (µm/s)	D_{TICS} (µm²/s)
1	6.2×10^{-3}	$(1.8 \pm 1.0)\times10^{-1}$	-1.8×10^{-5}	$(1.9 \pm 0.1)\times10^{-3}$	-2.4×10^{-3}	$(3.0 \pm 0.5)\times10^{-1}$	3.5×10^{-4}	$(1.3 \pm 0.2)\times10^{0}$
2	5.2×10^{-3}	$(1.8 \pm 0.8)\times10^{-1}$	-3.8×10^{-3}	$(9.6 \pm 1.2)\times10^{-4}$	-1.4×10^{-3}	$(7.1 \pm 0.8)\times10^{-4}$	9.0×10^{-4}	$(2.1 \pm 0.8)\times10^{0}$
3	5.1×10^{-3}	$(3.1 \pm 0.4)\times1^{0-1}$	-3.4×10^{-3}	$(2.8 \pm 0.3)\times10^{-3}$	-3.2×10^{-3}	$(9.7 \pm 0.6)\times10^{-4}$	-4.5×10^{-4}	$(3.1 \pm 1.0)\times10^{0}$
4	9.8×10^{-3}	$(1.3 \pm 0.1)\times10^{-3}$	-4.5×10^{-3}	$(1.2 \pm 0.1)\times10^{-3}$	-1.5×10^{-3}	$(8.1 \pm 0.2)\times10^{-4}$	-2.3×10^{-3}	$(2.4 \pm 1.8)\times10^{0}$
5	8.9×10^{-4}	$(2.3 \pm 0.2)\times10^{-3}$	-2.1×10^{-3}	$(2.6 \pm 1.0)\times10^{-1}$	-1.2×10^{-3}	$(5.4 \pm 1.6)\times10^{-1}$	-2.0×10^{-3}	$(1.3 \pm 2.4)\times10^{1}$
6	-2.4×10^{-3}	$(2.1 \pm 0.7)\times10^{-2}$	-2.4×10^{-3}	$(1.1 \pm 0.1)\times10^{-3}$	-1.6×10^{-3}	$(2.2 \pm 0.3)\times10^{-3}$	-2.0×10^{-4}	$(3.0 \pm 1.9)\times10^{0}$
7	4.5×10^{-3}	$(3.4 \pm 1.3)\times10^{-1}$	-1.9×10^{-3}	$(6.0 \pm 1.2)\times10^{-2}$	-3.0×10^{-3}	$(4.3 \pm 0.5)\times10^{-1}$	9.1×10^{-4}	$(1.8 \pm 0.4)\times10^{0}$
8	6.5×10^{-4}	$(6.7 \pm 8.2)\times10^{-2}$	-6.5×10^{-3}	$(3.4 \pm 2.2)\times10^{-1}$	1.2×10^{-3}	$(4.1 \pm 0.3)\times10^{-3}$	1.1×10^{-3}	$(4.2 \pm 0.6)\times10^{-1}$
9	2.2×10^{-3}	$(8.2 \pm 3.4)\times10^{-2}$	-2.5×10^{-3}	$(1.3 \pm 0.8)\times10^{-1}$	7.2×10^{-4}	$(1.3 \pm 0.1)\times10^{-3}$	8.1×10^{-4}	$(7.9 \pm 1.3)\times10^{-1}$
10	9.5×10^{-4}	$(8.3 \pm 5.7)\times10^{0}$	-5.6×10^{-3}	$(2.4 \pm 1.2)\times10^{-3}$	-2.7×10^{-4}	$(1.0 \pm 0.1)\times10^{-3}$	-2.6×10^{-4}	$(3.8 \pm 0.5)\times10^{-1}$
GM[a]	2.7×10^{-3}	7.9×10^{-2}	2.6×10^{-2}	2.0×10^{-3}	1.1×10^{-2}	1.8×10^{-3}	1.4×10^{-3}	7.4×10^{-3}
LCI 95%	1.4×10^{-3}	1.3×10^{-2}	2.7×10^{-3}	5.8×10^{-4}	1.7×10^{-3}	1.8×10^{-4}	7.9×10^{-4}	9.7×10^{-4}
UCl 95%	5.3×10^{-3}	4.9×10^{-1}	2.4×10^{-1}	6.7×10^{-3}	5.9×10^{-2}	1.2×10^{-2}	2.3×10^{-3}	5.6×10^{-2}

[a] *Geometric mean of the log-normal distribution.*

Treatment of live cells with nocodazole does not elicit drastic effects on the intracellular dynamics of NPs. From the Gaussian autocorrelation functions and their contour plots little decreases in flow velocities can be observed (*figure 15A-B*), which can also be confirmed from the flow mapping, showing smaller vectors. Although the magnitude has changed, the direction is still random. Because for each condition only three replicates are available, it is difficult to draw well-founded conclusions. Therefore more replicates are needed and the results obtained in this study are an indication. As explained earlier, ten regions are selected for each replicate. To give a clear overview, the geometric mean of the flow speed and diffusion coefficient is calculated for each replicate and the resulting mean of the three replicates is presented (*table 2*). These data approve the small diminishing dynamics of the NPs in cells after treatment with nocodazole. Regarding the diffusion coefficients, it is hard to draw reliable conclusions since the values are fluctuating strongly and high standard errors can be observed. The main reason for this problem is again the low number of replicates. Influences of nocodazole are very small as proven by the plot of the geometric means (*figure 17*). Furthermore Statistical analysis demonstrated no significant difference ($P > 0.05$) between the treated and untreated cells.

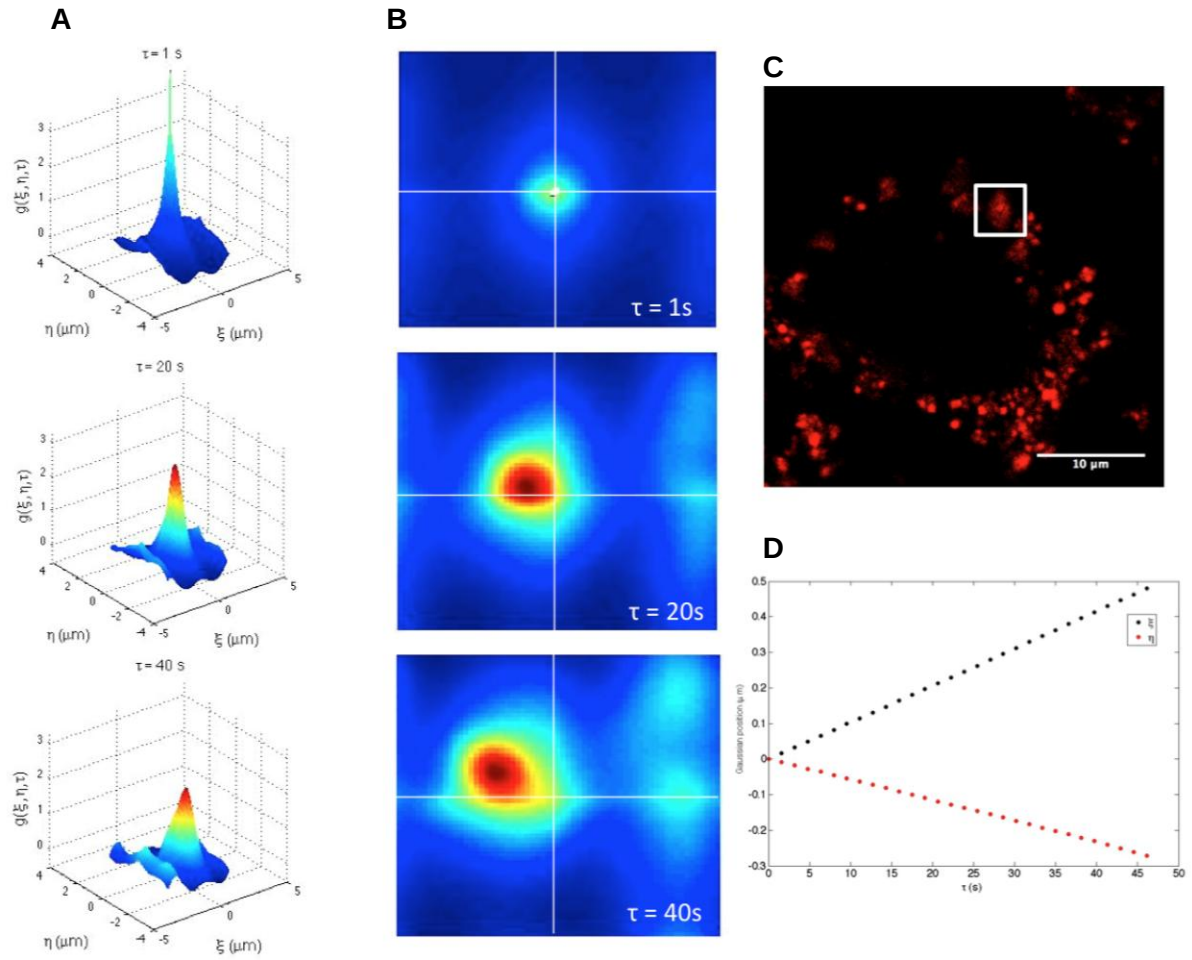

Figure 15: STICS analysis of a typical 64x64 pixels region of an A549 cell exposed for 4hrs to $BaTiO_3$ – France NPs functionalized with AMPA and treated with nocodazole*. For the selected region **(C)** the Gaussian autocorrelation functions $\boldsymbol{g(\xi,\eta,\tau)}$ **(A)** and their contour plot **(B)** after removal of immobile fraction are presented. For STICS and TICS analysis, 200 frames were collected without any time delay between sequential images. **(D)** Position of the $\boldsymbol{g(\xi,\eta,\tau)}$ peak as a function of time. Based on the peak position in time, an estimation of the concerted velocity of the particles ($2.38x10^{-2}$ µm/s) can be made.*

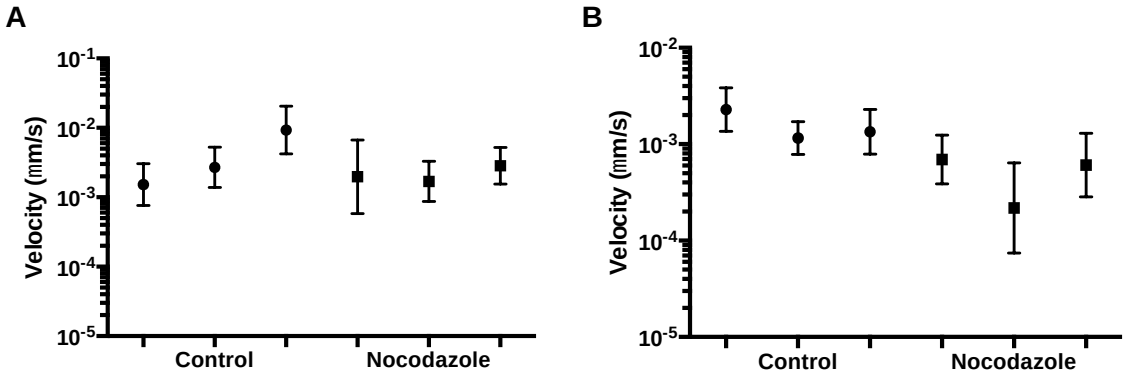

Figure 16: Geometric mean of flow velocities of $BaTiO_3$ NPs in A549 cells*. Plot of geometric means of velocities of flow measured using STICS analysis on A549 cells exposed to $BaTiO_3$ – France NPs functionalized with AMPA for 4 **(A)** and 24 hrs **(B)**. After exposure, part of the cells were treated with nocodazole. Each data-point represents the geometric mean of ten selected regions within one cell, to which STICS analysis is employed. Statistical analysis demonstrated no significant difference ($\boldsymbol{P} > 0.05$) between the treated and untreated cells.*

Table 2: Summarizing overview of flow velocities and diffusion coefficients for all conditions. *For each sample three replicates (cells) are analysed. For each replicate a geometric mean for the velocity of flow and magnitude of diffusion is obtained. Finally the mean and standard deviation of each set of three replicates is calculated and presented.*

	V_{STICS}	D_{TICS}
	Mean (10^{-3} µm/s)	Mean(10^{-2} µm/s)
France + AMPA 4hrs	4.5 ± 4.2	4.5 ± 3.3
France + AMPA 4hrs Nocodazole	2.8 ± 0.6	4.9 ± 5.3
France + AMPA 24hrs	1.6 ± 0.6	5.3 ± 7.9
France + AMPA 24hrs Nocodazole	0.5 ± 0.2	91 ± 68
France + citric acid 4hrs	0.6 ± 0.3	26 ± 21
France + citric acid 4hrs Nocodazole	0.3 ± 0.3	55 ± 50
France + citric acid 24hrs	2.7 ± 0.3	3.8 ± 3.7
France + citric 24hrs Nocodazole	0.5 ± 0.2	84 ± 86
Lee + AMPA 4hrs	1.2 ± 0.4	0.2 ± 0.2
Lee + AMPA 4hrs Nocodazole	0.8 ± 0.5	5.4 ± 0.3
Lee + AMPA 24hrs	1.4 ± 0.4	0.6 ± 0.1
Lee + AMPA 24hrs Nocodazole	1.1 ± 0.3	0.4 ± 0.2
Lee + citric acid 4hrs	1.5 ± 0.3	1.2 ± 1.4
Lee + citric acid 4hrs Nocodazole	1.5 ± 0.4	4.1 ± 3.0
Lee + citric acid 24hrs	0.9 ± 0.3	0.7 ± 0.3
Lee + citric acid 24hrs Nocodazole	1.5 ± 1.4	2.5 ± 2.4

To study the possible accumulation of $BaTiO_3$ NPs in cells and their co-localization with organelles, STICCS is a valuable tool. Therefore STICCS analysis of $BaTiO_3$ and lysosomes inside A549 cells is performed as a proof-of-principle. During imaging two different channels were used to image the SHG-signals from the NPs and the fluorescent signals emitted by the Lysotracker Green separately.

From the recorded image time series analysed with STICCS, a strong Gaussian correlation peak $g(\xi,\eta,\tau)$ can be seen (*figure 17D-E)*. While the broadening of the peak is rather null, meaning diffusion is very low, it appears to be mobile as a function of time. Information about the flow of the co-localized red and green populations (*figure 18A-B*) is obtained by fitting for the displacement of $g(\xi,\eta,\tau)$: V_{STICS} = 3.7x10^{-1} µm/s (v_x = 3.6x10^{-1}; v_y = -0.4x10^{-1} µm/s). Also for these data, the fact the NP-dispersion is unstable need to be considered. When NPs agglomerate and clusters of several hundreds of nanometer are formed together with protein absorption, they cannot be endocytosed by cellular vesicles. The NPs will be present at the outside of these structures but cannot be said to be inside.

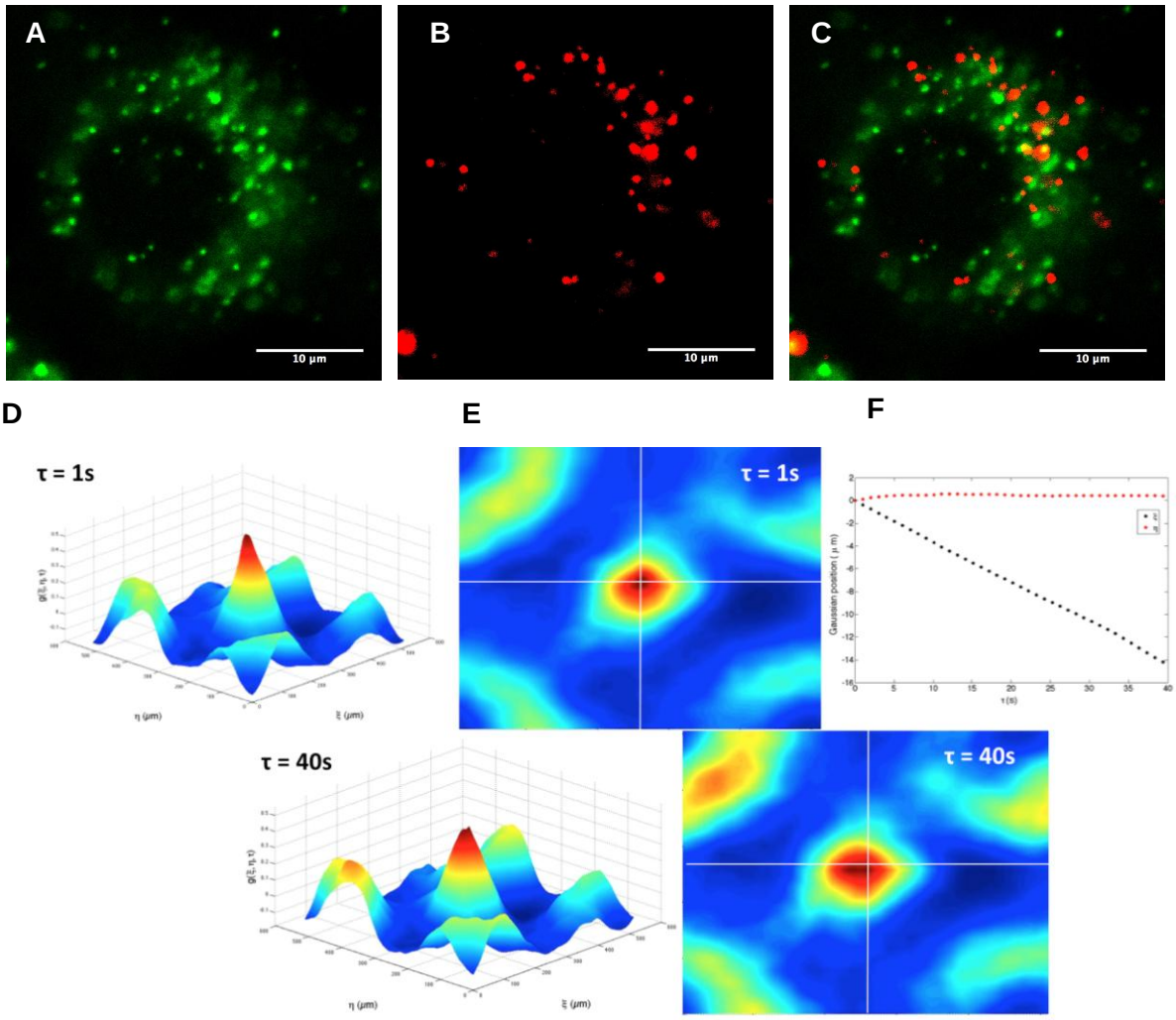

Figure 17: STICCS analysis of an A549 cell exposed to $BaTiO_3$ – Lee for 24 hrs and stained with lysotracker. *Gaussian autocorrelation function $g(\xi,\eta,\tau)$* ***(D)*** *and relating contour plots* ***(E)*** *(for τ = 1 and 40s) of $BaTiO_3$ – Lee NPs and lysotracker in an A549 cell obtained via cross-correlation (STICCS) analysis. The SHG signals from the NPs* ***(B)*** *and the fluorescence from the Lysotracker Green* ***(A)*** *are recorded in two channels. The overlay of both channels is presented in part* ***(C)****. For each channel 100 frames are recorded and correlated.* ***(F)*** *represents the position of the Gaussian peak $g(\xi,\eta,\tau)$ as a function of time τ, giving V_{STICS} = 3.7x10^{-1} µm/s (v_x = 3.6x10^{-1}; v_y = -0.4x10^{-1} µm/s)*

3.6 Intracellular motions studied by fluorescence anisotropy

To use the CLSM setup for anisotropy measurements, the system needed to be adjusted as described in section 2.6. To analyse anisotropy, fluorescent lifetime imaging was performed using two detectors. The detectors are used in T-format, where one detects the intensity coming from the horizontally polarized light and one detects intensities arising from the vertically polarized component. Based on these intensities, anisotropy can be calculated using Eq. (6). This formula contains the G-factor to correct for differences in sensitivity between both detectors. Since the goal of these measurements is proof-of-principle for the setup to construct anisotropy decay curves no values are needed. Therefore, equal sensitivity (G = 1) is assumed as a first approach. After setup adjustments were finished, testing measurements with R6G dissolved in a serial dilution of glycerol are performed. Glycerol is chosen because of its viscosity, which is tuned to create conditions from freely

moving R6G (0% glycerol) to almost completely fixed molecules (100% glycerol). For the anisotropy curves this would mean a sharp decay for 0% glycerol and a small decay in case of 100% glycerol.

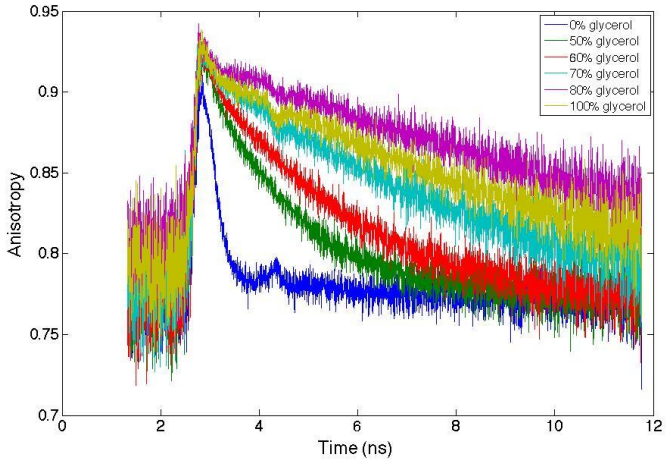

Figure 18: Anisotropy decay curves of Rhodamine 6G in glycerol dilutions

Calculating the anisotropy for the glycerol serial dilution reveals gradually changing decay curves as expected (*figure 18*). R6G dissolved in water (0% glycerol) has the sharpest decay in time while R6G dissolved in 100% glycerol gives rise to a curve with a less pronounced decay. For each anisotropy curve, the fundamental anisotropy is given by the peak value of the decay curve. The peak values of figure 18 lie between 0.9 and 0.95 and should give a measure for $r_0^{(2)}$. As reported by Ameloot et al. (2013), the fundamental anisotropy for R6G using two-photon excitation is 0.496 ± 0.011[35]. To obtain a fundamental anisotropy of 0.5, a value G somewhat larger than 5 is needed. This is a very high value and certainly greater than the indication of the G-value based on the following experiments. This is possibly caused by horizontal components contributing to the vertical polarized intensity. However, these experiments demonstrate the setup is working and further optimization can be carried out.

3.6.1 Determination of the G-factor

Time-resolved anisotropy is calculated using Eq. (6), which is complemented by the G-factor to correct for the differential sensitivity of the detection channels. Since the detection system is made out of two detectors, for vertically and horizontally polarized light respectively, the G-factor is simply given by the ratio of the sensitivity of both detectors (Eq. (7)). Determination of the variances in sensitivity between both detectors is done by means of circularly polarized light. In this case the intensity for both vertical and horizontal component is equal. Therefore both detectors should detect the same amount of photons. As a testing sample R6G is dissolved in water and in 60% glycerol. By using circularly polarized excitation light, both

detectors are expected to measure equal curves. When this is true, the vertical shift between both curves can be used to calculate the G-factor. However, the curves analysed in present experiments are not equal (*figure 19*).

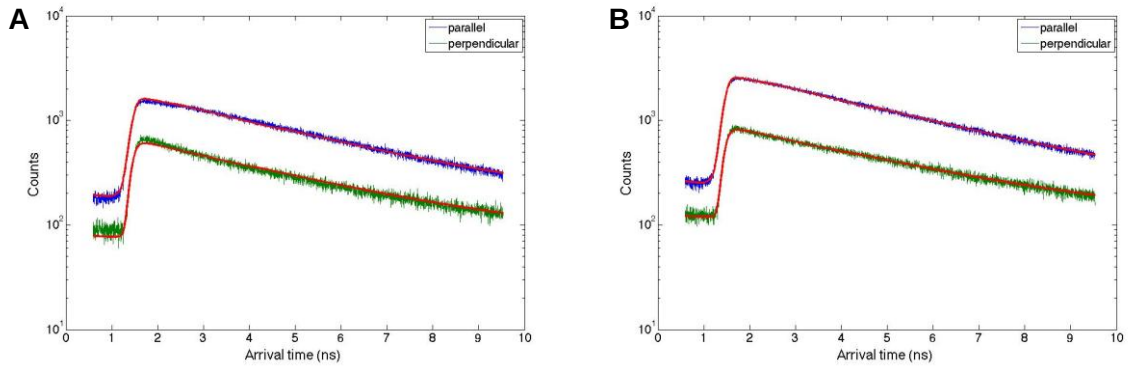

Figure 19: Fluorescence decay curves of R6G in water and glycerol using circularly polarized excitation light. *Amount of counted photons in time of R6G dissolved in 60% glycerol* ***(A)*** *and in water* ***(B)*** *after excitation with circularly polarized light. For each condition, the curves are plotted to a model and G values are determined.*

Differences in the flection of the curves can be seen, impeding the determination of the G-factor. Moreover, sample-dependent deviations are present, as can also be seen in the next experiments. Based on these experiments G-factors of 2.66 ± 0.01 for R6G in glycerol and 3.29 ± 0.01 for R6G in water are found, which are rather high.

3.6.2 Fine-tuning anisotropy measurement by analysing system-effects

To adjust the calculations for polarizing effects by the dichroic mirror, analysis of these diminishing effects is performed using a separate setup. In this setup a laser beam is pointed towards a rotatable polarizer, to produce a linearly polarized beam. After deflection by the dichroic mirror positioned at 45°, the beam is incident on a photo-diode, detecting the intensity. The photo-diode is positioned at an angle of 90° with respect to the laser source. The intensity of the laser beam is measured while rotating the polarizer in steps of 20°.

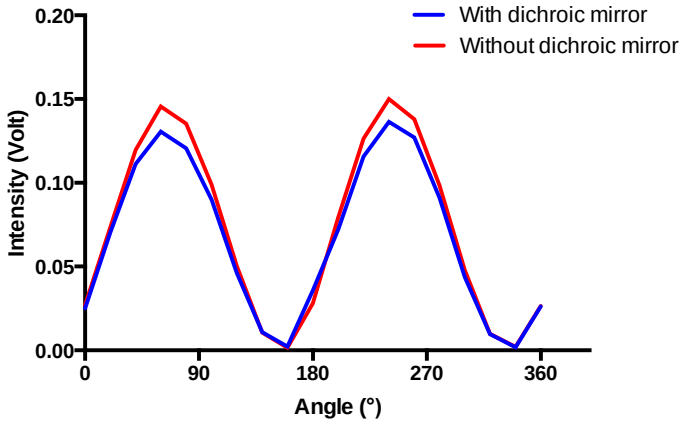

Figure 20: Influence of the dichroic mirror on the intensity, analysed using a rotatable polarizer

For each angle, 100 measurements were performed during 0.1s. The experiment was repeated after removal of the dichroic mirror from the optical path. Plotting the analysed intensities in function of the angle of the depolarizer (*figure 20*) reveals a small loss of intensity when the dichroic mirror is present. This loss of intensity due to the dichroic mirror is rather small, yet it has to be considered during calculating the anisotropy decay curves.

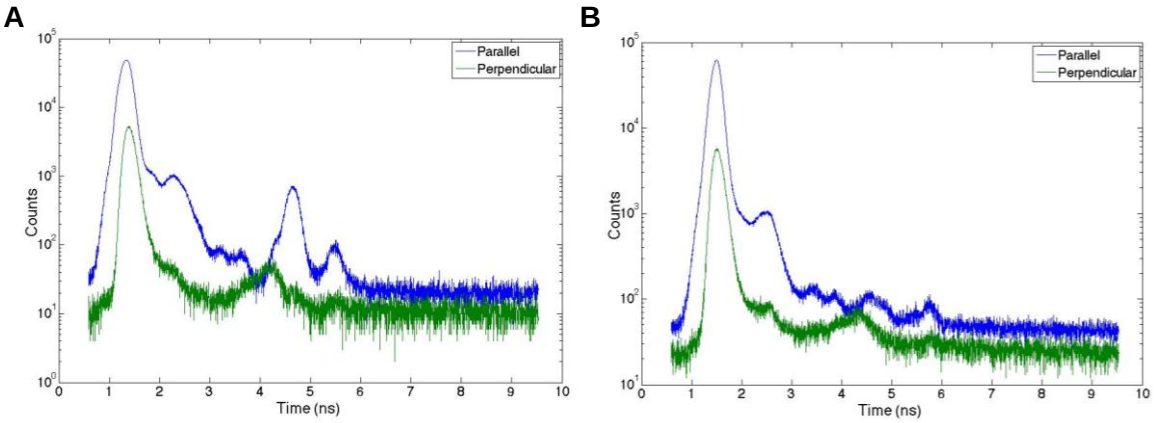

Figure 21: Instrument response functions of the CLSM setup. *With a KDP crystal as a sample, IRFs using a 10x Air objective* ***(A)*** *and a 40x water objective* ***(B)*** *were determined for the confocal setup used in for the fluorescence anisotropy study. For each IRF, the intensity of both channels, perpendicular (green) and parallel (blue) to the polarization direction of the excitation light, are measured.*

As fluorescence anisotropy is based on time-resolved fluorescence spectroscopy and FLIM data analysis in presence of SHG signals is performed, knowledge about the instrument response function (IRF) is required to record correct fluorescence lifetimes[56]. Since the FLIM procedure measures the convolution of the fluorescence decay curve with the IRF, correct lifetimes are obtained by de-convoluting the measured decay curves with the IRF[57].

In present study, a two photon pulsed laser source is used for fluorescent lifetime imaging. Therefore, a fast process, converting the excitation wavelength into the wavelength range of the fluorescence is needed to record the IRF. Because regular fluorescence has a lot of disadvantages and second-harmonic generation is an ultrafast process, SHG is preferred[57, 58]. Using KDP crystals, IRFs for each objective available (six in total) are measured using both horizontally and vertically polarized light (*figure 21*). These curves are taken into account in calculating and fitting of the anisotropy.

Investigation of the effects arising from rotation of the removable detectors demonstrate a very small angle-dependent effect (*figure 22*). For each data point (angle), a model is fitted to the experimental data. For each fit, the fundamental anisotropy, as well as the correlation time and the G-factor are obtained. The mean G-factor of the five data points is 8.72 ± 0.13, which is again a high value.

Ideally, a constant fundamental anisotropy and correlation time is expected upon rotating the detectors. Analysis of the fundamental anisotropy as a function of the detector angle reveals a quasi-horizontal line, just below 0.5 (*figure 22B*). This value is very close to the fundamental anisotropy for R6G (0.496 ± 0.011) as described by Ameloot et al. (2013). Slightly larger differences are observed for the correlation times (*figure 22A*). Comparing the obtained correlation times to the correlation time of R6G in propylene glycol (8.19 ± 0.69 ns) as reported by Ameloot et al. (2013), a small decrease can be seen. Since the rotational correlation times only depends on the hydrodynamic volume of the rotor, and on the temperature and viscosity of the solvent, the observed decrease can be attributed to the latter because the viscosity of glycerol is higher than the viscosity of propylene glycol. In general, rotation of the detectors has a minor effect on the anisotropy analysis. However, to avoid errors calibration is recommended each time detectors are replaced.

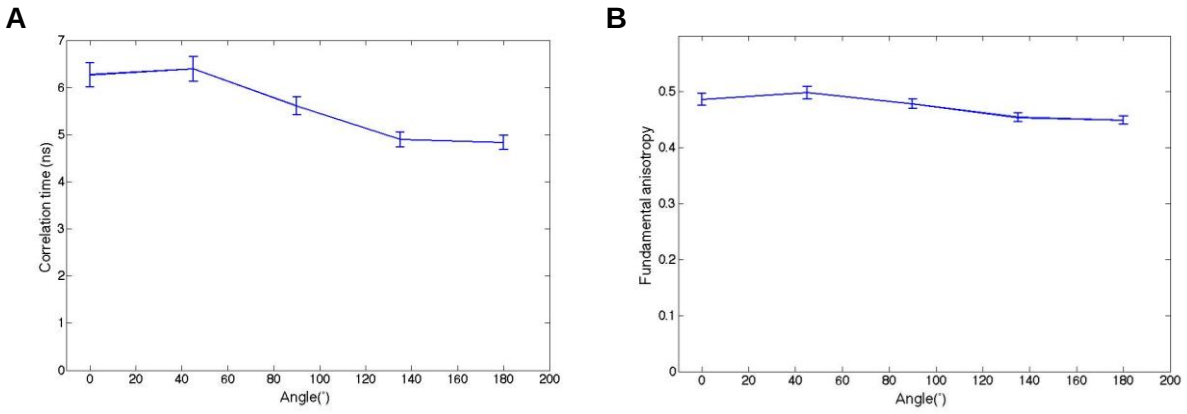

Figure 22: Plots of correlation time (A) and fundamental anisotropy (B) as a function of the angle of the detectors. *Polarizing influences from the detectors are tested by rotating the detectors and analysing the fundamental anisotropy and correlation time respectively of R6G in 100 v/v% glycerol.*

3.6.3 Fluorescence anisotropy applied on MRC-5 cells and fluorescently loaded polymers

Fluorescence anisotropy is applied to MRC-5 cells exposed to fluorescently loaded polymers. Since complete images of the cells are measured, each pixel of the image represents a decay curve for each detection channel. The curves representing the intensity-decays in both detection channels (*figure 24*) are therefore obtained by summing all the pixels from the image and fit a model to these experimental data. To compare the curves of the polymers loaded with a fluorescein derivative (*figure 24 B+D*) with the curves from the free fluorescein labels (*figure 24 A+C)* the rotational correlation time θ_j is used. Comparing the correlation time of free BiB-fluorescein (θ_j= 0.17 ± 0.02 ns) to the correlation time of the polymer loaded with BiB-fluorescein (θ_j= 0.28 ± 0.04 ns) reveals an increase. The same effect is observed when correlation times of free fluorescein acrylate (θ_j= 0.16 ± 0.03 ns) and of the polymer loaded with fluorescein acrylate (θ_j= 0.45 ± 0.04 ns) are compared. Since an increased correlation time is a consequence of a diminished rotational motion, as is observed for larger

molecules, the analyzed data demonstrate the ester-linkage is not affected by the cellular esterases, keeping the fluorescently loaded polymer intact. By fitting the decay curves, values for the fundamental anisotropy and for the G-factor are obtained (*table 3*). Very high G-values are obtained, while the values for r_0 appear normal[59].

Table 3: G-factor and fundamental anisotropy data obtained for the live cell experiments with polymers

Sample	r_0	G
Free BiB-fluorescein	0.53 ± 0.09	7.19 ± 0.11
BiB-fluorescein + polymer	0.50 ± 0.05	7.84 ± 0.17
Free fluorescein acrylate	0.43 ± 0.10	9.86 ± 0.17
Fluorescein acrylate + polymer	0.45 ± 0.04	11.11 ± 0.19

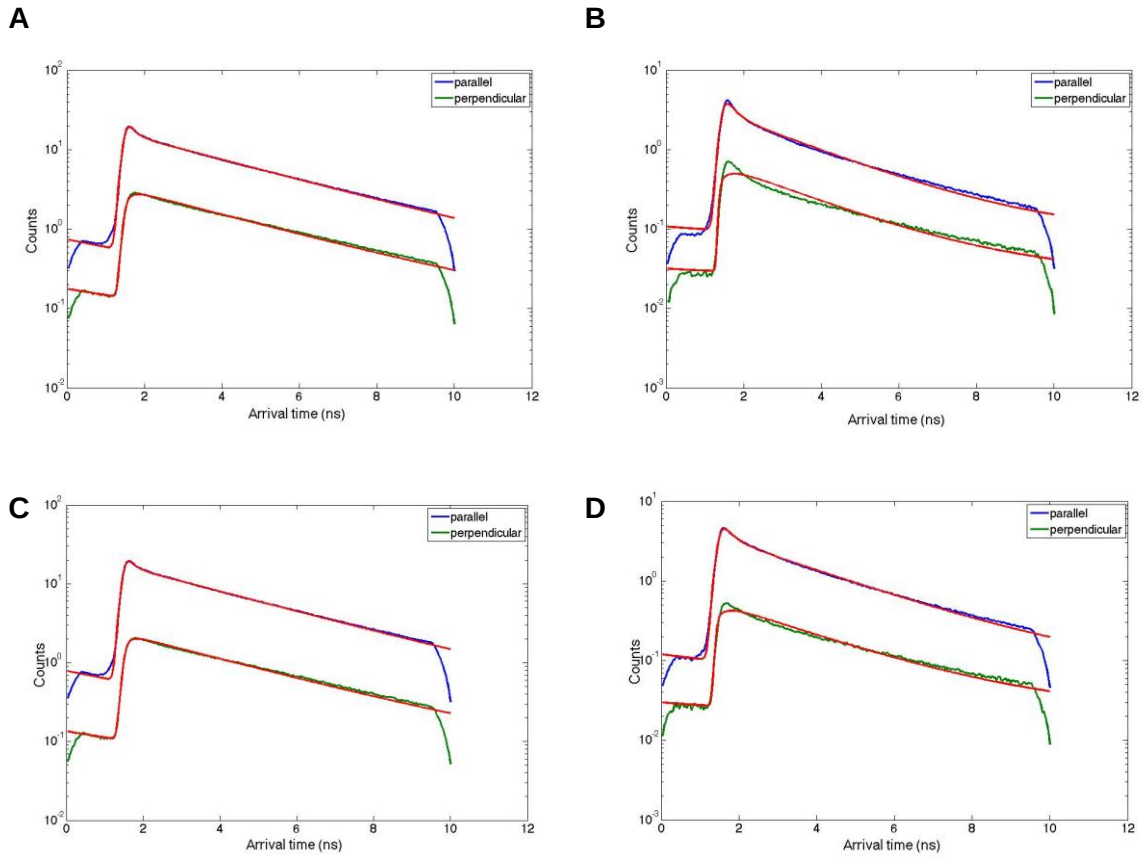

Figure 23: Decay curves of the fluorescent intensity as a function of time for MRC-5 cells. *MRC-5 cells are exposed to different polymers loaded with fluorescein:* ***(A)*** *control cells exposed to free BiB-fluorescein (**θ**$_j$= 0.17 ± 0.02 ns);* ***(B)*** *polymer loaded with BiB-fluorescein (**θ**$_j$= 0.28 ± 0.04 ns);* ***(C)*** *control cells exposed to free fluorescein acrylate (**θ**$_j$= 0.16 ± 0.03 ns);* ***(D)*** *polymer loaded with fluorescein acrylate (**θ**$_j$= 0.45 ± 0.04 ns). For each condition the intensity for the horizontal (blue) and vertical component (green) are measured as a function of time and are fitted.*

4 Conclusion

Since not much is known about the impact of NPs on living systems and literature is rather limited about dynamics of NPs in live cells, this study was set up. Previous studies and preliminary data led to the hypothesis that the intracellular fate of NPs is determined by the processes of uptake and transport. The main idea was to use optical imaging techniques to elucidate intracellular dynamics of $BaTiO_3$ NPs. On one hand, it was the aim to investigate diffusional and directed motions by means of image correlation spectroscopy and on the other hand to study the rotational motions of NPs using fluorescence anisotropy. For all the experiments the instability of the NP-dispersion as well the aggregation of the NPs need to be taken into account. However, it was established that $BaTiO_3$ NPs exert small toxic effects on living cells. Furthermore, using these NPs in live cell experiments revealed that the particles are endocytosed by these cells and are co-localized with the lysosomes. By means of STICS and TICS, intracellular movements are elucidated. Moreover, it was found that NPs both diffuse and move in a directed mode.

Immunocytochemistry revealed the disturbed tubulin network of the cells treated with nocodazole. Using this antimicrotuble agent, the contribution of the tubulin structures to cellular transport can be easily deduced. However perturbing the tubulin network does not significantly affects the intracellular transport of $BaTiO_3$. Labelling the same tubulin polymers was done by transfecting mturquoise2-plasmids. Although actin-filaments were clearly visible, tubulin required a lot of optimization and is still not successive, making this a future challenge.

Fluorescence anisotropy measurements were successfully implemented in the confocal setup of the host group. Moreover, anisotropy decay curves could be constructed using data collected based on the FLIM technique. For the calculation of the anisotropy, different influences from the system needed to be taken into account. Measurements showed a small intensity decrease by the dichroic mirror. Further, besides rotation of the detectors, differential sensitivity between both detector channels was studied. To correct for this difference in sensitivity, the G-factor is implemented in the equation for anisotropy. Next to a small dissimilarity between both channels, measurements have revealed the G-factor to be different between diverse measurements. Furthermore, rotation of the detectors demonstrate very small polarizing effects. Applying fluorescence anisotropy to live cell experiments worked well. Using rotational correlation times, rotational motions of the polymers were analyzed and effects of esterases on the bound between the polymer and fluorescent label could be studied.

Because today the dynamics of NPs are still poorly investigated, this study is one of the first in elucidating intracellular motions of NPs by means of optical method. Moreover, using SHG-active particles circumvents many problems optical imaging techniques, using fluorescent labels, are facing. However, this study has just thrown some light on this matter. In the future researching the dynamics and behaviour of NPs inside living systems need to be further employed. Possible next steps are a more extensive study of the flow and diffusion based on image correlation spectroscopy. Subsequent this can be extended to cross-correlation experiments to study co-localization of the NPs in different cell organelles. Therefore labels designed for early and late endosomes, lysosomes, mitochondria etc. are very valuable. Furthermore tubulin structures labelled by means of transfecting plasmids can be used as a mask to investigate the possible movements of NPs along these tracks. These experiments complemented by exclusion studies where inhibiting agents are used, could possibly reveal contribution of cytoskeletal structures and motor proteins to intracellular uptake and transport of NPs. Exclusion studies may even be able to demonstrate which mechanisms of uptake are of more importance. However before all the experiments above can be done, a thorough optimization of the starting materials need to be carried out. In other words, a stable dispersion of NPs without aggregation and clustering need to be obtained. Moreover a comprehensive characterization of these NPs is fundamental to be able to draw reliable conclusions regarding cellular effects and dynamics.

Regarding the fluorescence anisotropy technique, a lot of hurdles are successfully taken. Determination of the differential sensitivity of the detector channels was however less evident than expected. Although using circularly polarized light was valuable for the calculation of the G-factor, measurement dependent G-values were detected. Additionally the values for G obtained during the experiments are very high. This leads to the conclusion that horizontal components are contributing to the vertical polarized intensity. In other words, this cannot be corrected by the G-factor that only corrects for different sensitivity in the two detection channels. When fluorescence anisotropy is fully optimized for this system, it can be applied to fluorescent NPs to study their rotational dynamics. Using these data together with the results from the ICS measurements can be a big step towards the elucidation of the intracellular dynamics of NPs. Successful studies will be of major importance in nanomedicine, since they will contribute to the optimization of drug delivery systems. Moreover they will be helpful in the development of safe nano-products.

5 References

1. Buzea C, Pacheco, II, Robbie K. Nanomaterials and nanoparticles: sources and toxicity. Biointerphases. 2007;2:Mr17-71.
2. Vert M, Doi Y, Hellwich K-H, Hess M, Hodge P, Kubisa P, et al. Terminology for biorelated polymers and applications (IUPAC Recommendations 2012). Pure and Applied Chemistry. 2012;84(2).
3. Vercauteren D, Rejman J, Martens TF, Demeester J, De Smedt SC, Braeckmans K. On the cellular processing of non-viral nanomedicines for nucleic acid delivery: mechanisms and methods. Journal of controlled release : official journal of the Controlled Release Society. 2012;161:566-81.
4. Panariti A, Miserocchi G, Rivolta I. The effect of nanoparticle uptake on cellular behavior: disrupting or enabling functions? Nanotechnology, Science and Applications. 2012;5:87-100.
5. Xia T, Li N, Nel AE. Potential health impact of nanoparticles. Annual review of public health. 2009;30:137-50.
6. Ivanov AI. Pharmacological inhibition of endocytic pathways: is it specific enough to be useful? Methods in molecular biology (Clifton, NJ). 2008;440:15-33.
7. Ha SW, Weitzmann MN, Beck GR. Bio-Active Silica Nanoparticles Promote Osteoblast Differentiation Though Stimulation of Autophagy and Direct Association with LC3 and p62. ACS nano. 2014.
8. Kettiger H, Schipanski A, Wick P, Huwyler J. Engineered nanomaterial uptake and tissue distribution: from cell to organism.International journal of nanomedicine. 2013;8:3255-69.
9. Cordonnier M, Dauzonne D, Louvard D, Coudrier E. Actin Filaments and Myosin I Alpha Cooperate with microtubules for the movement of lysosomes. Molecular biology of the cell. 2001;12:4013-29.
10. Gheshlaghi ZN, Riazi GH, Ahmadian S, Ghafari M, Mahinpour R. Toxicity and interaction of titanium dioxide nanoparticles with microtubule protein. Acta biochimica et biophysica Sinica. 2008;40:777-82.
11. Peachman KK, Rao M, Palmer DR, Zidanic M, Sun W, Alving CR, et al. Functional microtubules are required for antigen processing by macrophages and dendritic cells. Immunology letters. 2004;95:13-24.
12. Xu F, Piett C, Farkas S, Qazzaz M, Syed NI. Silver nanoparticles (AgNPs) cause degeneration of cytoskeleton and disrupt synaptic machinery of cultured cotrical neurons. Molecular Brain. 2013;6.
13. Gupta AK, Gupta M, Yarwood SJ, Curtis AS. Effect of cellular uptake of gelatin nanoparticles on adhesion, morphology and cytoskeleton organisation of human fibroblasts. Journal of controlled release : official journal of the Controlled Release Society. 2004;95(2):197-207.
14. Ciofani G, Danti S, Moscato S, Albertazzi L, D'Alessandro D, Dinucci D, et al. Preparation of stable dispersion of barium titanate nanoparticles: Potential applications in biomedicine. Colloids and surfaces B, Biointerfaces. 2010;76(2):535-43.
15. Lee H-W, Moon S, Choi C-H, Kim DK, Kang SJ. Synthesis and Size Control of Tetragonal Barium Titanate Nanopowders by Facile Solvothermal Method. Journal of the American Ceramic Society. 2012;95(8):2429-34.
16. Mao Y, Mao S, Ye Z-G, Xie Z, Zheng L. Solvothermal synthesis and Curie temperature of monodispersed barium titanate nanoparticles. Materials Chemistry and Physics. 2010;124(2-3):1232-8.
17. Ciofani G, Ricotti L, Canale C, D'Alessandro D, Berrettini S, Mazzolai B, et al. Effects of barium titanate nanoparticles on proliferation and differentiation of rat mesenchymal stem cells. Colloids and surfaces B, Biointerfaces. 2013;102:312-20.
18. Staedler D, Magouroux T, Hadji R, Joulaud C, Extermann J, Schwung S, et al. Harmonic nanocrystals for biolabeling: a survey of optical properties and biocompatibility. ACS nano. 2012;6:2542-9.

19. Rao M. Barium Titanate, BaTiO3 Visakhapatnam2013. Available from: http://www.gitam.edu/eresource/Engg_Phys/semester_2/dielec/BaTiO3.htm.
20. Pantazis P, Maloney J, Wu D, Fraser SE. Second harmonic generating (SHG) nanoprobes for in vivo imaging. Proceedings of the National Academy of Sciences of the United States of America. 2010;107:14535-40.
21. Campagnola PJ, Loew LM. Second-harmonic imaging microscopy for visualizing biomolecular arrays in cells, tissues and organisms. Nature biotechnology. 2003;21(11):1356-60.
22. Hsieh C-L, Grange R, Pu Y, Psaltis D. Three-dimensional harmonic holographic microcopy using nanoparticles as probes for cell imaging. 2009.
23. Hebert B, Costantino S, Wiseman PW. Spatiotemporal image correlation spectroscopy (STICS) theory, verification, and application to protein velocity mapping in living CHO cells. Biophys J. 2005;88(5):3601-14.
24. Hebert B, Costantino S, Wiseman PW. Spatiotemporal image correlation spectroscopy (STICS) theory, verification, and application to protein velocity mapping in living CHO cells. Biophys J. 88. United States2005. p. 3601-14.
25. Magde D, Webb WW, Elson E. Thermodynamic fluctuations in a reacting system - measurement by fluorescence correlation spectroscopy. Physical Review Letters. 1972;29:705-&.
26. Petersen NO, Hoddelius PL, Wiseman PW, Seger O, Magnusson KE. Quantitation of membrane receptor distributions by image correlation spectroscopy: concept and application. Biophys J. 1993;65(3):1135-46.
27. Wiseman PW. Image correlation spectroscopy: mapping correlations in space, time, and reciprocal space. Methods in enzymology. 2013;518:245-67.
28. Elson EL. Fluorescence correlation spectroscopy: past, present, future. Biophys J. 101. United States: 2011 Biophysical Society. Published by Elsevier Inc; 2011. p. 2855-70.
29. Brown CM, Dalal RB, Hebert B, Digman MA, Horwitz AR, Gratton E. Raster image correlation spectroscopy (RICS) for measuring fast protein dynamics and concentrations with a commercial laser scanning confocal microscope. J Microsc. 2008;229(Pt 1):78-91.
30. Bajzer Z, Moncrieffe MC, Penzar I, Prendergast FG. Complex homogeneous and heterogeneous fluorescence anisotropy decays: enhancing analysis accuracy. Biophys J. 2001;81(3):1765-75.
31. Lidke DS, Nagy P, Barisas BG, Heintzmann R, Post JN, Lidke KA, et al. Imaging molecular interactions in cells by dynamic and static fluorescence anisotropy (rFLIM and emFRET). Biochem Soc Trans. 2003;31(Pt 5):1020-7.
32. Lakowicz JR. Principles of fluorescence spectroscopy. Third ed. Baltimore, Maryland, USA: Springer; 2006.
33. Lakowicz JR. Topics in Fluorescence Spectroscopy Volume 5 Nonlinear and Two-Photon-Induced Fluorescence. New York1997.
34. Ameloot M, vandeVen M, Acuna AU, Valeur B. Fluorescence anisotropy measurements in solution: Methods and reference materials (IUPAC Technical Report). Pure and Applied Chemistry. 2013;85(3):589-608.
35. Ameloot M, vandeVen M, Acuna AU, Valeur B. Fluorescence anisotropy measurements in solution: Methods and reference materials (IUPAC Technical Report). Pure and Applied Chemistry. 2013;85:589-608.
36. Goedhart J, von Stetten D, Noirclerc-Savoye M, Lelimousin M, Joosen L, Hink MA, et al. Structure-guided evolution of cyan fluorescent proteins towards a quantum yield of 93%. Nature communications. 2012;3:751.
37. Reveron H, Aymonier C, Loppinet-Serani A, Elissalde C, Maglione M, Cansell F. Single-tep synthesis of well-crystallized and pure barium titanate nanoparticles in supercritical fluids. Nanotechnology. 2005;16:1137-43.
38. Jordan M, Thrower D, Wilson L. Effects of vinblastine, podophyllotoxin and nocodazole on mitotic spindles. Journal of Cell Science. 1992.
39. Smisdom N. The dynamic behvior of the glycine receptor in the plasma membrane. Diepenbeek: Hasselt University; 2011.

40. Kolin DL, Wiseman PW. Advances in image correlation spectroscopy: measuring number densities, aggregation states, and dynamics of fluorescently labeled macromolecules in cells. Cell biochemistry and biophysics. 2007;49(3):141-64.
41. Penjweini R, Smisdom N, Deville S, Ameloot M. Transport and accumulation of PVP-Hypericin in cancer and normal cells characterized by image correlation spectroscopy techniques. Biochimica et biophysica acta. 2014.
42. Hebert B, Costantino S, Wiseman PW. Spatiotemporal image correlation spectroscopy (STICS) theory, verification, and application to protein velocity mapping in living CHO cells. Biophysical journal. 2005;88:3601-14.
43. Wiseman PW, Squier JA, Ellisman MH, Wilson KR. Two-photon image correlation spectroscopy and image cross-correlation spectroscopy. Journal of microscopy. 2000;200:14-25.
44. Comeau JWD, Kolin DL, Wiseman PW. Accurate measurements of protein interactions in cells via improved spatial image cross-correlation spectroscopy. Molecular BioSystems. 2008;4(6):672-85.
45. Maiorano G, Sabella S, Sorce B, Brunetti V, Ada Malvindi M, Cingolani R, et al. Effects of Cell Culture Media on the Dynamic Formation of Protein-Nanoparticle Complexes and Influence on the Cellular Response. ACS nano. 2010;12:7481-91.
46. Shen ZG, Chen JF, Zou HK, Yun J. Dispersion of nanosized aqueous suspensions of barium titanate with ammonium polyacrylate. Journal of colloid and interface science. 2004;275(1):158-64.
47. Wang YH, Li KJ, Mao L, Hu X, Zhao WJ, Hu A, et al. Effects of exogenous zinc on cell cycle, apoptosis and viability of MDAMB231, HepG2 and 293 T cells. Biological trace element research. 2013;154(3):418-26.
48. Faust JJ, Zhang W, Chen Y, Capco DG. Alpha-Fe(2)O(3) elicits diameter-dependent effects during exposure to an in vitro model of the human placenta. Cell biology and toxicology. 2014;30(1):31-53.
49. Alberts B, Johnson A, Lewis J, Raff M, Roberts K, Walter P. Molecular Biology of The Cell, Fifth Edition. New York: Garland Science, Taylor & Francis Group; 2008.
50. Sun W, Gu Y, Wang G, Fang N. Dual-modality single particle orientation and rotational tracking of intracellular transport of nanocargos.Analytical chemistry. 2012;84(2):1134-8.
51. Peltier S, Oger JM, Lagarce F, Couet W, Benoit JP. Enhanced oral paclitaxel bioavailability after administration of paclitaxel-loaded lipid nanocapsules. Pharmaceutical research. 2006;23(6):1243-50.
52. Chen J, Horwitz S. Differential Mitotic Responses to Microtubule-stabilizing and -destabilizing Drugs. Cancer Research. 2002;62:1935-8.
53. Morel E, Parton RG, Gruenberg J. Annexin A2-dependent polymerization of actin mediates endosome biogenesis. Developmental cell. 2009;16(3):445-57.
54. Huber F, Schnauss J, Ronicke S, Rauch P, Muller K, Futterer C, et al. Emergent complexity of the cytoskeleton: from single filaments to tissue. Advances in physics. 2013;62(1):1-112.
55. Vasquez RJ, Howell B, Yvon AM, Wadsworth P, Cassimeris L. Nanomolar concentrations of nocodazole alter microtubule dynamic instability in vivo and in vitro. Molecular biology of the cell. 1997;8(6):973-85.
56. Szabelski M, Luchowski R, Gryczynski Z, Kapusta P, Ortmann U, Gryczynski I. Evaluation of instrument response functions for lifetime imaging detectors using quenched Rose Bengal solutions. Chemical Physics Letters. 2009;471(1-3):153-9.
57. Becker W. The bh TCSPC Handbook 2012.
58. Becker W. Recording the Instrument Response Function of a Multiphoton FLIM System 2012.
59. Jameson DM, Ross JA. Fluorescence polarization/anisotropy in diagnostics and imaging. Chemical reviews. 2010;110(5):2685-708.

6 Appendix

6.1 Structure of fluorescein labels

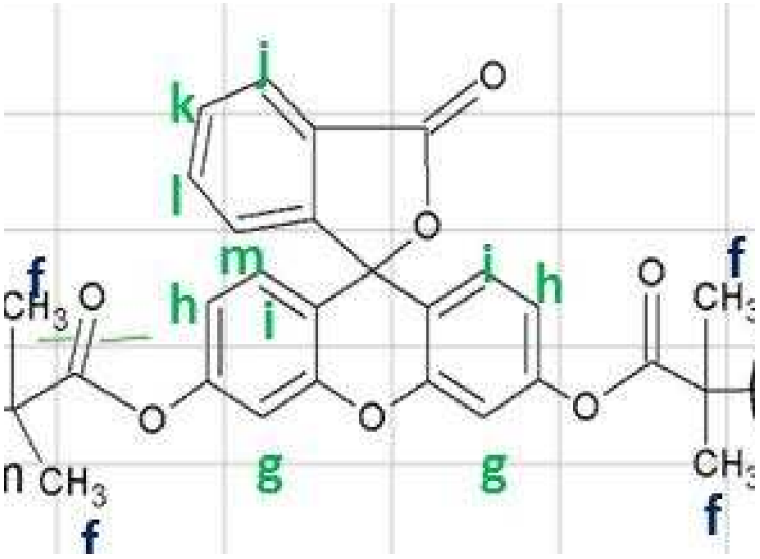

Figure A.1: Structure of BiB-Fluorescein

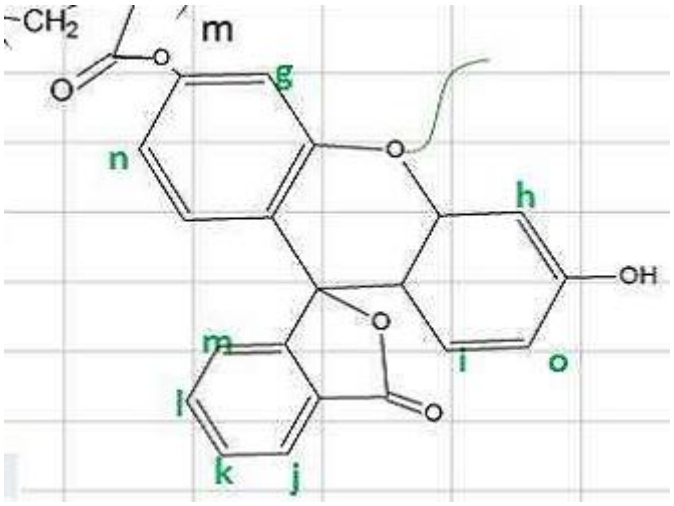

Figure A.2: Structure of Fluorescein Acrylate

6.2 Plasmid primers

For the sequencing three forward primers (PV30, SD1, SD2) and one reverse primer (GM1) were used. The primers are designed in a way there is always an overlap with the subsequent primer to ensure no parts of the sequence is skipped (*Figure A.3 + A.4*).

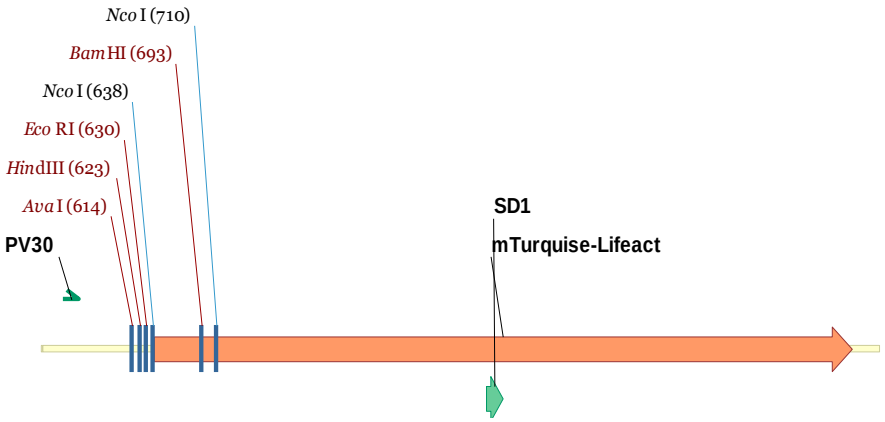

Figure A.3: Fragment of pLifeAct-mTurquoise2 (Addgene 36201), 950 bp (molecule 4765 bp)

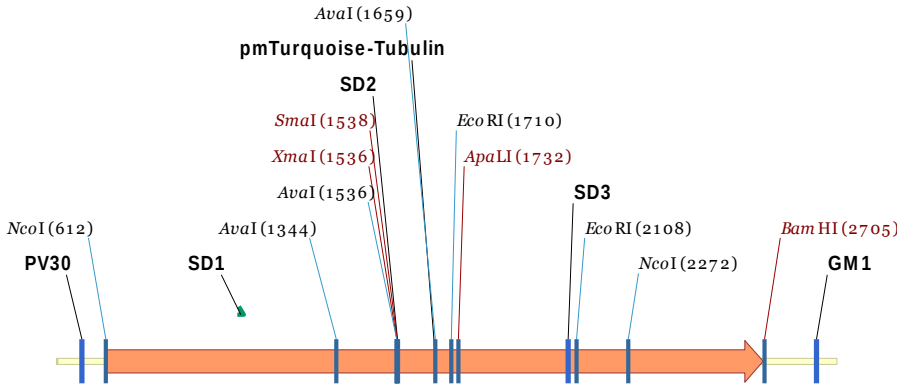

Figure A.4: Fragment of pmTurquoise2-Tubulin (Addgene 36202), 2476 bp (molecule 6045 bp)

6.3 Plasmid sequences

6.3.1 pLifeAct-mTurquoise2

154211_B10_4630001_lifeAct-mTurq2_PV30_078
GACGTCAGATCCGCTAGCGCTACCGGACTCAGATCTCGAGCTCAAGCTTCGAATTCCACCATGGGCGTGGC
CGACCTGATCAAGAAGTTCGAGAGCATCAGCAAGGAGGAGGGGGATCCACCGGTCGCCACCATGGTGAGCA
AGGGCGAGGAGCTGTTCACCGGGGTGGTGCCCATCCTGGTCGAGCTGGACGGCGACGTAAACGGCCACAAG
TTCAGCGTGTCCGGCGAGGGCGAGGGCGATGCCACCTACGGCAAGCTGACCCTGAAGTTCATCTGCACCAC
CGGCAAGCTGCCCGTGCCCTGGCCCACCCTCGTGACCACCCTGTCCTGGGGCGTGCAGTGCTTCGCCCGCT
ACCCCGACCACATGAAGCAGCACGACTTCTTCAAGTCCGCCATGCCCGAAGGCTACGTCCAGGAGCGCACC
ATCTTCTTCAAGGACGACGGCAACTACAAGACCCGCGCCGAGGTGAAGTTCGAGGGCGACACCCTGGTGAA
CCGCATCGAGCTGAAGGGCATCGACTTCAAGGAGGACGGCAACATCCTGGGGCACAAGCTGGAGTACAACT
ACTTTAGCGACAACGTCTATATCACCGCCGACAAGCAGAAGAACGGCATCAAGGCCAACTTCAAGATCCGC
CACAACATCGAGGACGGCGGCGTGCAGCTCGCCGACCACTACCAGCAGAACACCCCCATCGGCGACGGCCC
CGTGCTGCTGCCCGACAACCACTACCTGAGCACCCAGTCCAAGCTGAGCAAAGACCCCAACGAGAAGCGCG
ATCACATGGTCCTGCTGGAGTTCGTGACCGCCGCCGGGATCACTCTCGGCATGGACGAGCTGTACAAGTAA
AGCGGCCGCGACTCTAGATCATAATCAGCCATACCACATTTGTAGAGGTTTTACTTGCTTTAAAAAACCTC
CCACACCTCCCCCTGAACCTGAAACATAAAATGAATGCA

>153304_C12_4599354_lifeAct-mTurq2_SD1_092
CGGCATCAAGGCCAACTTCAAGATCCGCCACAACATCGAGGACGGCGGCGTGCAGCTCGCCGACCACTACC
AGCAGAACACCCCCATCGGCGACGGCCCCGTGCTGCTGCCCGACAACCACTACCTGAGCACCCAGTCCAAG
CTGAGCAAAGACCCCAACGAGAAGCGCGATCACATGGTCCTGCTGGAGTTCGTGACCGCCGCCGGGATCAC
TCTCGGCATGGACGAGCTGTACAAGTAAAGCGGCCGCGACTCTAGATCATAATCAGCCATACCACATTYGT
AGAGGTTTTACTTMGCTTTAAAAAACCTCCCACACCTCCCCCTGAACCTGAAACATAAAATGAATGCAATT
YGTTGTTGTTAACTTYGTTTATTGCAGCTTATAATGGTTACAAATAAAGCAATAGCATCACAAATTTCACA
AATAAAGCATTTTTTTCACTGCATTCTAGTTGTGGTTTGTCCAAACTCATCAATGTATCTTAAGGCGTAAA
TTGTAAGCGTTAATATTTTGTTAAAATTCGCGTTAAATTTTTGTTAAATCAGCTCATTTTTTAACCAATAG
GCCGAAATCGGCAAAATCCCTTATAAATCAAAAGAATAGACCGAGATAGGGTTGAGTGTTGTTCCAGTTTG
GGAACAAGAGTCCACTATTAAAGAACGTGGACTCCAACGTCAAAGGGCGAAAAACCGTCTATCAGGGCGAT
GGCCCACTACGTGAACCATCACCCTAATCAAGTTTTTTGGGGTCGAGGTGCCGTAAAGCACTAAATCGGAA
CCCTAAAGGGAGCCCCCGATTTAGAGCTTGACGGGAAAGCCGGCGAACGTGGCGAGAAAGGAAGGG

6.3.2 pmTurquoise2-Tubulin

>154211_C10_4630002_mTurq2-Tubulin_PV30_076
CCGCTAGCGCTACCGGTCGCCACCATGGTGAGCAAGGGCGAAGGAGCTGTTCACCGGGGWGGTGCCCATCC
TGGTCGAGCTGGACGGCGACGTAAACGGCCACAAGTTCAGCGTGTCCGGCGAGGGCGAGGGCGATGCCACC
TACGGCAAGCTGACCCTGAAGTTCATCTGCACCACCGGCAAGCTGCCCGTGCCCTGGCCCACCCTCGTGAC
CACCCTGTCCTGGGGCGTGCAGTGCTTCGCCCGCTACCCCGACCACATGAAGCAGCACGACTTCTTCAAGT
CCGCCATGCCCGAAGGCTACGTCCAGGAGCGCACCATCTTCTTCAAGGACGACGGCAACTACAAGACCCGC
GCCGAGGTGAAGTTCGAGGGCGACACCCTGGTGAACCGCATCGAGCTGAAGGGCATCGACTTCAAGGAGGA
CGGCAACATCCTGGGGCACAAGCTGGAGTACAACTACTTTAGCGACAACGTCTATATCACCGCCGACAAGC
AGAAGAACGGCATCAAGGCCAACTTCAAGATCCGCCACAACATCGAGGACGGCGGCGTGCAGCTCGCCGAC
CACTACCAGCAGAACACCCCCATCGGCGACGGCCCCGTGCTGCTGCCCGACAACCACTACCTGAGCACCCA
GTCCAAGCTGAGCAAAGACCCCAACGAGAAGCGCGATCACATGGTCCTGCTGGAGTTCGTGACCGCCGCCG
GGATCACTCTCGGCATGGACGAGCTGTACAAGTCCGGACTCAGATCTCGAGTGCGTGAGTGCATCTCCATC
CACGTTGGCCAGGCTGGTGTCCAGATTGGCAATGCCTGCTGGGAGCTCTACTGCCTGGAACACGGCATCCA
GCCCGATGGCCAGATGCCAAGTGACAAGACCAT

>153304_E12_4599356_mTurq2-Tubulin_SD1_088
AGCAGAAGACGGCATCAAGGCCAACTTCAAGATCCGCCACAACATCGAGGACGGCGGCGTGCAGCTCGCCG
ACCACTACCAGCAGAACACCCCCATCGGCGACGGCCCCGTGCTGCTGCCCGACAACCACTACCTGAGCACC
CAGTCCAAGCTGAGCAAAGACCCCAACGAGAAGCGCGATCACATGGTCCTGCTGGAGTTCGTGACCGCCGC

CGGGATCACTCTCGGCATGGACGAGCTGTACAAGTCCGGACTCAGATCTCGAGTGCGTGAGTGCATCTCCA
TCCACGTTGGCCAGGCTGGTGTCCAGATTGGCAATGCCTGCTGGGAGCTCTACTGCCTGGAACACGGCATC
CAGCCCGATGGCCAGATGCCAAGTGACAAGACCATTGGGGGAGGAGATGACTCCTTCAACACCTTCTTCAG
TGAGACGGGCGCTGGCAAGCACGTGCCCCGGGCTGTGTTTGTAGACTTGGAACCCACAGTCATTGATGAAG
TTCGCACTGGCACCTACCGCCAGCTCTTCCACCCTGAGCAGCTCATCACAGGCAAGGAAGATGCTGCCAAT
AACTATGCCCGAGGGCACTACACCATTGGCAAGGAGATCATTGACCTTGTGTTGGACCGAATTCGCAAGCT
GGCTGACCAGTGCACCGGTCTTCAGGGCTTCTTGGTTTTCCACAGCTTTGGTGGGGGAACTGGTTCTGGGT
TCACCTCCCTGCTCATGGAACGTCTCTCAGTTGATTATGGCAAGAAGTCCAAGCTGGAGTTCTCCATTTAC
CCAGCACCCCAGGTTTCCACAGCTGTAGTTGAGCCCTACAACTCCATCCTCACCACCCACACCACCCT

>153304_F12_4599357_mTurq2-Tubulin_SD2_086
GTTGGACCGAATTCGCAAGCTGGCTGACCAGTGCACCGGTCTTCAGGGCTTCTYGGTTTTCCACAGCTTTG
GTGGGGGAACTGGTTCTGGGTTCACCTCCCTGCTCATGGAACGTCTCTCAGTTGATTATGGCAAGAAGTCC
AAGCTGGAGTTCTCCATTTACCCAGCACCCCAGGTTTCCACAGCTGTAGTTGAGCCCTACAACTCCATCCT
CACCACCCACACCACCCTGGAGCACTCTGATTGTGCCTTCATGGTAGACAATGAGGCCATCTATGACATCT
GTCGTAGAAACCTCGATATCGAGCGCCCAACCTACACTAACCTTAACCGCCTTATTAGCCAGATTGTGTCC
TCCATCACTGCTTCCCTGAGATTTGATGGAGCCCTGAATGTTGACCTGACAGAATTCCAGACCAACCTGGT
GCCCTACCCCCGCATCCACTTCCCTCTGGCCACATATGCCCCTGTCATCTCTGCTGAGAAAGCCTACCATG
AACAGCTTTCTGTAGCAGAGATCACCAATGCTTGCTTTGAGCCAGCCAACCAGATGGTGAAATGTGACCCT
CGCCATGGTAAATACATGGCTTGCTGCCTGTTGTACCGTGGTGACGTGGTTCCCAAAGATGTCAATGCTGC
CATTGCCACCATCAAAACCAAGCGCAGCATCCAGTTTGTGGGATTGGTGCCCCACTGGCTTCAAGGTTGGC
ATCA

>153304_G12_4599358_mTurq2-Tubulin_GM1_084
ATCCTTAGTATTCCTCTCCTTCTTCCTCACCCTCTCCTTCAACAGAATCCACACCAACCTCCTCATAATCC
TTCTCAAGGGCAGCCATATCTTCACGGGCCTCTGAAAACTCGCCTTCCTCCATCCCCTCACCCACGTACCA
GTGAACAAAGGCACGCTTMGGCATACATCAGGTCAAACTTGTGGTCCAGGCGAGCCCAGGCCTCAGCAATG
GCTGTGGTGTTGCTCAGCATGCACACAGCTCTCTGTACCTTWGGCCAGGTCTCCACCAGGCACCACAGTGG
GAGGCTGGTAGTTGATGCCAACCTTGAAGCCAGTGGGGCACCAATCCACAAACTGGATGCTGCGCTTKGGT
TTTGATGGTGGCAATGGCAGCATTGACATCTTTGGGAACCACGTCACCACGGTACAACAGGCAGCAAGCCA
TGTATTTACCATGGCGAGGGTCACATTTCACCATCTGGTTGGCTGGCTCAAAGCAAGCATTGGTGATCTCT
GCTACAGAAAGCTGTTCATGGTAGGCTTTTCTCAGCAGAGATGACAGGGGCATATGTGGCCAGAGGGAAGT
GGATGCGGGGGTAGGGCACCAGGTTGGTCTGGAATTCTGTCAGGTCAACATTCAGGGCTCCATCAAATCTC
AGGGAAGCAGTGATGGAG

6.4 Formulas of ICS

Two-dimensional diffusion:

$$g(0,0,\tau) = \boldsymbol{g}(\mathbf{0},\mathbf{0},\mathbf{0})\left(1+\frac{\tau}{\boldsymbol{\tau_d}}\right)^{-1} + \boldsymbol{g}_\infty \qquad \text{A.1}$$

Two dimensional flow:

$$g(0,0,\tau) = \boldsymbol{g}(\mathbf{0},\mathbf{0},\mathbf{0})\exp\left\{-\left(\frac{|\boldsymbol{V_f}|\tau}{\langle\omega_{2p}\rangle}\right)^2\right\} + \boldsymbol{g}_\infty \qquad \text{A.2}$$

Two dimensional diffusion and flow for a single population:

$$g(0,0,\tau) = \boldsymbol{g}(\mathbf{0},\mathbf{0},\mathbf{0})\left(1+\frac{\tau}{\boldsymbol{\tau_d}}\right)^{-1} \times \exp\left\{-\left(\frac{|\boldsymbol{V_f}|\tau}{\langle\omega_{2p}\rangle}\right)^2\left(1+\frac{\tau}{\boldsymbol{\tau_d}}\right)^{-1}\right\} + \boldsymbol{g}_\infty \qquad \text{A.3}$$

Two dimensional diffusion and flow for two populations:

$$g(0,0,\tau) = \boldsymbol{g}(\mathbf{0},\mathbf{0},\mathbf{0})_1\left(1+\frac{\tau}{\boldsymbol{\tau_{d1}}}\right)^{-1} + \boldsymbol{g}(\mathbf{0},\mathbf{0},\mathbf{0})_2\exp\left\{-\left(\frac{|\boldsymbol{V_{f2}}|\tau}{\langle\omega_{2p}\rangle}\right)^2\right\} + \boldsymbol{g}_\infty \qquad \text{A.4}$$

With the mean speed of the particles $|\boldsymbol{V_f}|$ the characteristic flow time τ_f can be calculated by:

$$|\boldsymbol{V_f}| = \frac{\omega_{2p}}{\tau_f} \qquad \text{A.5}$$

where ω_{2p} is a parameter determined by the optics of the set-up. Using the diffusion decay time τ_d, the diffusion coefficient can be calculated by:

$$D_{exp} = \frac{\langle\omega_{2p}\rangle^2}{4\boldsymbol{\tau_d}} \qquad \text{A.6}$$

Auteursrechtelijke overeenkomst

Ik/wij verlenen het wereldwijde auteursrecht voor de ingediende eindverhandeling:
Optical imaging of intracellular dynamics of nanoparticles in live cells

Richting: **master in de biomedische wetenschappen-bio-elektronica en nanotechnologie**
Jaar: **2014**

in alle mogelijke mediaformaten, - bestaande en in de toekomst te ontwikkelen - , aan de Universiteit Hasselt.

Niet tegenstaand deze toekenning van het auteursrecht aan de Universiteit Hasselt behoud ik als auteur het recht om de eindverhandeling, - in zijn geheel of gedeeltelijk -, vrij te reproduceren, (her)publiceren of distribueren zonder de toelating te moeten verkrijgen van de Universiteit Hasselt.

Ik bevestig dat de eindverhandeling mijn origineel werk is, en dat ik het recht heb om de rechten te verlenen die in deze overeenkomst worden beschreven. Ik verklaar tevens dat de eindverhandeling, naar mijn weten, het auteursrecht van anderen niet overtreedt.

Ik verklaar tevens dat ik voor het materiaal in de eindverhandeling dat beschermd wordt door het auteursrecht, de nodige toelatingen heb verkregen zodat ik deze ook aan de Universiteit Hasselt kan overdragen en dat dit duidelijk in de tekst en inhoud van de eindverhandeling werd genotificeerd.

Universiteit Hasselt zal mij als auteur(s) van de eindverhandeling identificeren en zal geen wijzigingen aanbrengen aan de eindverhandeling, uitgezonderd deze toegelaten door deze overeenkomst.

Voor akkoord,

Wathiong, Bart

Datum: **9/06/2014**